ERROR CHARACTERIZATION FOR AIRBORNE CLOUD PROBES USING LABORATORY CALIBRATION AND IN-SITU ANALYSIS

Spencer Faber

A thesis submitted to the Department of Atmospheric Science and the University of Wyoming in partial fulfillment of the requirements for the degree of

MASTER OF SCIENCE
in
ATMOSPHERIC SCIENCE

June 2017

Faber, Spencer, Error characterization for airborne cloud probes using laboratory calibration and in-situ analysis, MS Department of Atmospheric Science, June, 2017

Measurements of cloud liquid water content and droplet size distributions are essential for studies of cloud microphysical processes and cloud radiative properties. The Nevzorov hotwire probe provides measurements of cloud liquid and total water content by monitoring the amount of power required to maintain element temperature while cloud particles are evaporated. Factors including convective heat losses, collection efficiency considerations, and sensor saturation can introduce uncertainty in Nevzorov measurements. Nevzorov calculations include reference sensor power and a convective heat loss coefficient to compensate for convective heat losses. The convective heat loss coefficient is dependent on airspeed and density. Changes in airspeed or flight level result in Nevzorov liquid and total water content baseline drift. A convective heat loss calibration method that uses UWKA calibration flight data is developed and tested. Validation of the calibration method provides estimates of minimum detectable liquid/total water content and estimates of uncertainty caused by convective heat losses.

The Cloud Droplet Probe (CDP) is a single particle counter that provides measurements of droplet size distributions, droplet concentration, and liquid water content. Inhomogeneity in laser beam intensity, optical component misalignment, and uncertainty in measurements of sample area result in counting and sizing error. A droplet generating calibration system was developed to test sizing and counting

accuracy at discrete locations across the sample area and provide measurements of sample area size.

Nevzorov and CDP measurements collected during the Precipitation and Cloud Measurements for Instrument Characterization and Evaluation (PACMICE) and Seeded and Natural Orographic Wintertime clouds – the Idaho Experiment (SNOWIE) campaigns are analyzed. Nevzorov uncertainty is evaluated for examples of liquid cloud, ice cloud, mixed phase cloud, and drizzle conditions. Comparisons of Nevzorov and CDP liquid water content are used to further investigate uncertainty sources affecting both instruments.

Table of Contents

List of Tables

Chapter 2

Chapter 3

List of Figures

Chapter 2

Chapter 3

Chapter 4

1. Importance of in-situ cloud measurements

Clouds are complex, highly dynamic systems that are influenced by processes that act on time and spatial scales that span orders of magnitude. It is necessary to better understand clouds, and the various processes that influence them, for many reasons. Such knowledge is required to develop more accurate precipitation forecasts which are essential for agricultural operations, urban planning, natural resource management, and predicting extreme precipitation events (Taylor, et al., 2016). Studies of cloud processes are also central to more accurately modeling cloud radiative interactions which are dependent on many factors including cloud phase, cloud temperature, particle size, and particle concentration (Zelinka, et al., 2012). The sheer complexity of radiative interactions has made the development of accurate cloud radiative models a daunting task. Difficulties in modeling cloud radiative interactions are among the main factors contributing to global climate model disagreement (Zelinka, et al., 2012).

Aircraft based in-situ measurements of cloud properties are essential components of many cloud studies because they provide measurements of state and cloud properties on fine spatial scales. In-situ measurements of cloud liquid water content (LWC) provide a constraint on the amount of water mass available to produce precipitation. LWC is also a central component of bulk cloud models that are used to simulate cloud evolution and interactions with other Earth System components (Morrison and Gettelman, 2008).

Measurements of LWC are commonly provided by two classes of airborne instruments. Constant temperature hotwire probes, including the LWC-100, King, Nevzorov, and Scientific Engineering Applications (SEA) probes, feature heated elements that are subject to cloud particle impact. For these probes, the sensing element is maintained at a fixed temperature near 100 C so that impinging particles are evaporated. Evaporation requires energy be transferred from the element to impinging particles. As a result, additional power must be supplied in order to maintain a constant element temperature. LWC measurements are obtained by relating the power supplied to the element, the latent heat of vaporization for water, and the element's sample volume (King et al., 1978). Historically, hotwire probes were capable of measuring only LWC but the more recently-developed Nevzorov and SEA probes feature multiple heated elements that can independently provide measurements of LWC and total condensed cloud water content (TWC) (Korolev et al., 1998, Emery, et al., 2004). Furthermore, cloud ice water content (IWC) can be calculated by differencing TWC and LWC.

Optical Particle Counting (OPC) probes, such as the Forward Scattering Spectrometer Probe (FSSP) and Cloud Droplet Probe (CDP), are also capable of providing measurements of LWC (Baumgardner, 1983; Lance et al., 2010). OPCs utilize an open path laser and photodetectors to count and size cloud droplets. As the probes are passed through cloud, droplets intercept the laser beam and forward scatter photons; some of which are collected and focused onto photodetectors. Detector response and Mie scattering theory are related to provide measurements of droplet size.

Measurements of droplet count and size provide Droplet Size Distributions (DSDs) that are integrated to obtain measurements of LWC. (Dye and Baumgardner, 1984)

DSDs are essential for studies of cloud microphysical characteristics, processes, and radiative properties. Characteristically, newly-formed clouds have relatively small mean droplet diameter because LWC is small and vertical development is limited. DSDs are relatively narrow because droplets in young clouds primarily grow through condensation (Kohler, 1936; Squires, 1952; Mason and Chien, 1962).

Condensational growth alone cannot grow droplets to precipitation sized particles within the timescales observed in nature. Collision/coalescence is a process that can quickly grow droplets to precipitation sized particles (Blanchard, 1950; Bowen, 1950; Scott, 1968). Collision/coalescence acts to decrease cloud optical depth because it decreases droplet concentration more than it increases the second DSD moment. Coalescent growth is inefficient for narrow DSDs found in newly formed clouds because droplets have similar terminal velocities and are unlikely to contact one another.

Entrainment, or the turbulent mixing of environmental air, impacts cloud characteristics during all stages of cloud evolution. The process is the dominate factor that limits cloud lifetime because the introduction of sub-saturated air acts to evaporate cloud particles (Warner, 1973). Entrainment can alter DSDs in many different manners depending on the relationship between evaporative and mixing timescales (Baker, 1980; Blyth, 1992). At one extreme, homogenous mixing occurs when evaporative timescales are much

greater than mixing timescales. Homogenous mixing will decrease droplet diameter in a relatively uniform manner. In contrast, inhomogeneous mixing occurs when evaporative timescales are much less than mixing timescales and causes greater variation in the decrease of droplet diameter (Baker, 1980; Blyth, 1992). Inhomogeneous mixing broadens DSDs which creates conditions more favorable for droplet growth by collection/coalescent processes.

Mixed phase processes also have important impacts on cloud characteristics and cloud evolution. Saturation vapor pressure is lower over ice than it is over liquid water which causes ice particles to grow by deposition (Wegener, 1911; Bergeron, 1935; Findeisen, 1938). Under many circumstances, ice particle size will increase while droplet size simultaneously decreases. Ice particle concentration greatly influences precipitation production rates in mixed phase environments. The Hallett-Mossop process (also known as rime splintering) is capable of rapidly producing high concentrations of small ice particles in certain temperature regimes (Mossop, 1970; Mossop and Hallett, 1974; Koenig and Murray, 1977). Small crystals generated through the Hallett-Mossop process can subsequently act to rapidly glaciate cloud.

The Nevzorov and CDP are subject to several sources of uncertainty. A considerable amount of work has focused on Nevzorov uncertainty sources including collection efficiency effects, sensor saturation, and convective heat losses (Korolev et al., 1998; Strapp et al., 2003; Schwarzenboeck et al., 2009). Many factors contribute to CDP uncertainty including optical component misalignment (Lance et al., 2010 and 2012),

uncertainty in sample volume dimensions (Baumgardner, 1983, Dye and Baumgardner, 1984), and coincidence error (Baumgardner et al., 1985, Cooper, 1988, Brenguier, 1988).

It can be difficult to investigate Nevzorov and CDP uncertainty in both natural and laboratory settings. Natural studies are complex because it is not possible to control the highly variable conditions found in clouds. In-situ studies also require independent measurements be provided by other instruments; which are themselves subject to uncertainty. Laboratory studies are often limited by our ability to reproduce conditions found in natural settings. It can be especially difficult to produce precisely sized ice particles with crystal structures that mimic those found in clouds (Strapp, et al., 2003).

This thesis explores major factors that may lead to error in Nevzorov and CDP measurements and presents methods to investigate and minimize the impact of such factors. It is organized into three main chapters. One chapter will explore a calibration method designed to minimize Nevzorov uncertainty caused by convective heat losses. The second chapter will focus on a laboratory-based calibration method designed to investigate several factors that potentially compromise CDP measurements. A final chapter will explore additional uncertainty sources that affect the Nevzorov and CDP. It will incorporate results from the first two chapters and intercomparisons of LWC measured by both instruments.

2. The Nevzorov hotwire probe

This chapter discusses Nevzorov operating principles and explores convective heat losses which introduce uncertainty in Nevzorov water content measurements. It also presents a calibration method designed to minimize uncertainty related to convective heat losses and explores the effectiveness of the method. Additional uncertainty sources that affect Nevzorov measurements are discussed in Chapter 4.

2.1 – Nevzorov operating principles

The Nevzorov is a constant temperature hotwire probe that provides measurements of LWC and TWC utilizing thermodynamic principles and the latent heat consumed during the evaporation of cloud particles (Korolev et al., 1998). Figure 2.1 shows Nevzorov sensing head components that include a moveable vane to decrease uncertainty due to variations of aircraft angle of attack and four heated wire elements (hereafter called sensors). Two collector sensors are located on the leading edge of the vane so that they interact with cloud particles. The LWC collector is rod-shaped and is designed to interact with liquid particles only. Ice is expected to shatter and be swept away before significant particle/sensor interaction occurs. The TWC collector is an inverted cone and is designed to capture both liquid and ice particles. Sensor temperature is maintained at a constant value (selectable to be 90 - 110 C) so that impinging particles are evaporated. The latent heat associated with particle evaporation and (to a lesser extent) the sensible heat required to warm particles to the point of vaporization transfers energy from the collector sensors. $\mathrm{TWC}/\mathrm{LWC}$ measurements are calculated by relating the

amount of power required to maintain sensor temperature and fundamental thermodynamic principles. The two reference sensors are located on the trailing edge of the vane so that particle interaction is minimized. Reference sensor power signal is used to determine power consumption due to convective heat losses which would otherwise lead to an overestimation of LWC and TWC.

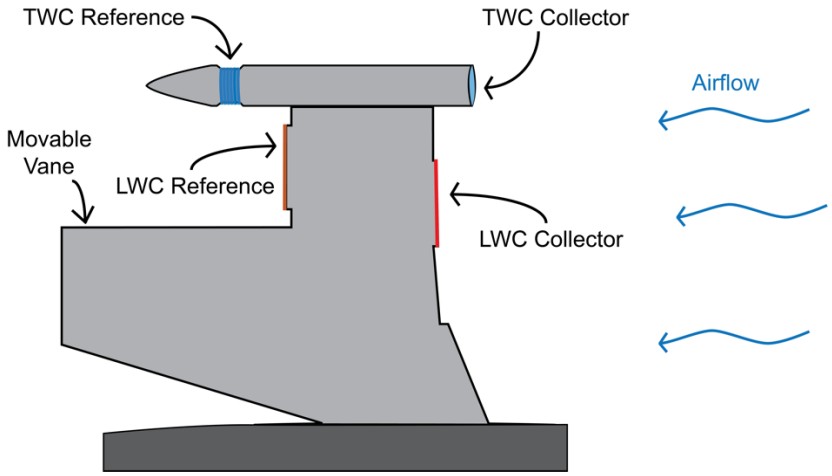

Figure 2.1 - *Schematic of the Nevzorov probe that shows the placement of the rod-shaped* LWC *collector and reference sensors (shown in red and brown) and the* TWC *collector and reference sensors (sky blue and blue). The* TWC *collector sensor is an "inverted cone" design and the* TWC *reference is in the form of a wound coil. Airflow and cloud particles would be traveling right to left.*

Basic operating principles and formulas used to calculate LWC and TWC are outlined in the manufacture's operating manual (SkyPhysTech, "Operating Manual Nevzorov hot wire LWC / TWC Probe"). Sensor power consumption due to cloud particle evaporation is

$$P = V_{col} * I_{col} - k * V_{ref} * I_{ref} \quad (2.1)$$

where V_{col} and V_{ref} are collector and reference sensor voltages, I_{col} and I_{ref} are sensor currents, and k is the convective heat loss coefficient.

LWC and TWC are related to P through:

$$LWC\ \&\ TWC = \frac{P}{e * U_{true} * S * L_w} \tag{2.2}$$

where e is collection efficiency (often assumed to be unity), U_{true} denotes true airspeed, S is collector sensor surface area, and L_w is the heat expended for the vaporization of liquid water, which is defined as

$$L_w = (T_{nev} - T) * 4.218 + 1918.46 * \left(\frac{T_{nev}}{T_{nev} - 33.91}\right)^2 \tag{2.3}$$

L_w is a form of the Nevzorov manual's "expanded heat for water" (L_W^*) formula (SkyPhysTech, "Operating Manual Nevzorov hot wire LWC / TWC Probe"). T_{nev} is the Nevzorov operating temperature and T is static temperature (both in Kelvin). The first term is the energy required to increase the temperature of liquid particles to T_{nev}; the point of vaporization. 4.218 is the specific heat of liquid water at 273.15 K with units of J g^{-1} K^{-1}. The second term is a temperature dependent parameterization of the latent heat of vaporization for liquid water (units are J g^{-1}) from Henderson and Sellers (1984).
Note: The second term in L_W could simply be replaced with the latent heat of vaporization at 100 C (2250.0 J g^{-1}) but the simplification introduces ~5% uncertainty in water content measurements.

Using L_w for TWC calculations neglects the fact that sensible and latent heats are dependent on particle phase. Nonetheless, L_w is used in TWC calculations because the fraction of liquid to ice particle mass is unknown.

In *ice phase cloud*, TWC can be calculated as

$$TWC = \frac{P_{TWC}}{e * U_{true} * S * L_i} \quad (2.4)$$

P_{TWC} is equation 2.1 with TWC reference and collector sensor power. L_i is the heat expended for the melting and vaporization of ice particles:

$$L_i = (273.15 - T) * 2.106 + (T_{nev} - 273.15) * 4.218 + 333.5 + 1918.46 * \left(\frac{T_{nev}}{T_{nev} - 33.91}\right)^2 \quad (2.5)$$

T and T_{nev} are expressed in Kelvin and each term in Li has resulting units of J g^{-1}. The first term in Li accounts for the energy required to increase ice particle temperature to the point of melting. The second term is the energy required to increase the melted particle temperature to the temperature of the collector sensor (T_{nev}). The third term is the energy expended in melting ice particles (the latent heat of fusion) and the final term represents the latent energy required to evaporate the melted ice particles (Henderson and Sellers, 1984).

In an ice phase cloud with static temperature of -20 C, calculating TWC using L_W, instead of L_i, would cause an 11% overestimation of TWC. The difference between L_i and L_W at a static temperature of 0 C shows that using L_W for TWC in mixed-phase and ice cloud would introduce at most 12% TWC uncertainty. A weighting of L_w and L_i could

be used to calculate mixed-phase TWC if the ratio of liquid to ice particle mass is known, but such information is rarely available.

2.2 - A Method to minimize LWC and TWC uncertainty caused by convective heat loss coefficient (k) drift

The convective heat loss coefficient (k) in Equation 2.1 accounts for the fact that convective heat losses are not equal for the collector and reference sensors. In clear air, LWC collector power is typically 40% greater than LWC reference power. The LWC collector and reference sensors have the same geometric design but flow passing the LWC reference sensor has been disturbed by the vane. The Reynolds number in the vicinity of the LWC reference sensor is within the turbulent flow regime (~340,000) when calculated using a characteristic velocity of 100 m s^{-1} and the kinematic viscosity of dry air at -10 C. Turbulent flow decreases LWC reference sensor convective heat losses.

In contrast to the LWC sensors, TWC reference sensor power is typically 20% greater than TWC collector power in clear air. The TWC collector and reference sensors have similar surface areas but different geometrical designs. The inverted cone shape of the TWC collector results in significant streamline divergence and turbulent conditions within the sensor which decreases TWC collector sensor convective heat losses relative to reference sensor losses (Korolev et al., 2013).

The convective heat loss coefficient (k) in Equation 2.1 varies with airspeed and, to a lesser extent, density (Korolev et al., 1998). In-flight variations of airspeed or flight level can cause k fluctuations on the order of 10% which in turn affects the accuracy of TWC and LWC measurements. TWC/LWC uncertainty due to k drift is evident as clear air drift in baseline TWC/LWC and can compromise Nevzorov measurements, especially in regions of low water content. In clear air, k is defined as the ratio of collector and reference sensor power

$$k = \frac{V_{col} * I_{col}}{V_{ref} * I_{ref}} \tag{2.4}$$

Several methods have been used to compensate for drift in baseline TWC/LWC caused by variations in k. For a study of cirrus ice particle properties, Cotton et al. (2013) compensated for k drift by linearly parameterizing how clear air TWC changes with change in true airspeed, static pressure, static temperature, and aircraft angle of attack. The researchers concluded that their baseline compensation method allowed for TWC measurements accurate to within ±0.001 g m^{-3} (Cotton et al., 2013).

A flight group at the University of North Dakota (UND) compensated for k drift by linearly parameterizing how k varies with changes of indicated airspeed and static pressure (McFarquhar et al., 2017). k relationships were calculated using clear air data on a flight-by-flight basis. Estimates of baseline accuracy were not provided by the UND group.

A method similar to the one used by the UND researchers is developed to compensate for k drift affecting the UWKA Nevzorov. Our method also employs parameterizations of k dependence on indicated airspeed and static pressure but does not require k relationships to be recalculated for individual flights. Instead, data used to develop k parameterizations are provided by a dedicated calibration flight. Calibrations consist of clear air maneuvers that include four legs flown at separate levels (typically 400, 500, 600, and 700 mb) that each contain four discrete sections of constant indicated airspeed (around 60, 70, 80, and 90 m s^{-1}). A subset that contains 60 1-second data points is manually selected from each period. It is unclear to what degree k is affected by changes in roll, sideslip, or angle of attack so care is taken to only include periods of straight and level flight. A first-degree surface fit of the following form is then used to estimate the relationship between k, indicated airspeed, and static pressure. The surface fit uses indicated, instead of true, airspeed because indicated airspeed in not affected by changes of density.

$$k = (A) * P_{stat} + (B) * U_{ind} + (C) \quad (2.5)$$

A is the pressure coefficient, B is an indicated airspeed coefficient, C is an intercept parameter, P_{stat} is static pressure, and U_{ind} is indicated airspeed. This surface fit provides a lookup table for estimating k over the entire range of airspeed and pressure encountered during typical UWKA operations.

2.3 - An evaluation of calibration performance

Six separate parameterizations of k (three for the LWC sensors and three for the TWC sensors) are determined from calibrations flown for the Wyoming Cloud Radar Test

(WCR), Precipitation and Cloud Measurements for Instrument Characterization and Evaluation (PACMICE), and a test flight for the Seeded and Natural Orographic Wintertime clouds – the Idaho Experiment (SNOWIE) campaigns. The WCR, PACMICE, and SNOWIE calibration flights occurred on 03/04/16, 08/18/16, and 12/08/16 respectively. Calibration flight names will hereafter be abbreviated as WCR, PAC, and SNOWIE.

2.3.1 – General TWC k calibration characteristics

Table 2.1 shows surface fit coefficients, r^2, and root mean squared error (RMSE) for the TWC k calibrations. The three TWC calibrations show similar trends of k vs. P_{stat} and k vs. U_{ind}; as indicated by the similarity of the fit coefficients. Fit statistics show that the surface fit most closely models k_{TWC} vs. P_{stat}/ U_{ind} trends for the WCR and PAC calibrations; both of which have r^2 near 0.99 and RMSE near 0.005. The fit applied to SNOWIE k_{TWC} produces a smaller r^2 (0.97) and RMSE that is nearly a factor of two greater than RMSE for the WCR and PAC fits. Figure 2.2 shows SNOWIE k_{TWC} vs. P_{stat} and k_{TWC} vs. U_{ind} relationships. The SNOWIE calibration's poorer fit statistics can be attributed to relationships between 500 mb k_{TWC}, U_{ind}, and P_{stat} that are significantly different than those observed at other flight levels.

Table 2.1 - *Fit coefficients and goodness-of-fit statistics for k_{TWC} fits applied to data from each calibration flight. P_{stat} coef., U_{ind} coef, and intercept parameter correspond to the A, B, and C parameters in equation 2.5.*

Calibration	P_{stat} coef. (A) [mb^{-1}]	U_{ind} coef. (B) [m^{-1} s]	Intercept parameter (C)	r^2	Root Mean Squared Error
WCR	$-3.47*10^{-4}$	$-4.73*10^{-3}$	1.42	0.9940	0.0044
PAC	$-4.13*10^{-4}$	$-4.34*10^{-3}$	1.43	0.9917	0.0055
SNOWIE	$-4.32*10^{-4}$	$-4.09*10^{-3}$	1.40	0.9700	0.0101

k_{TWC} calculated from the 500 mb leg shows less U_{ind} dependence; as illustrated in Figure 2.2a. The 500 mb k_{TWC} vs. U_{ind} slope (listed in upper right corner of Figure 2.2a) is approximately half the magnitude of the 700, 600, and 400 mb slopes.

500 mb k_{TWC} is also less dependent on P_{stat}. Figure 2.2b shows how 500 mb k_{TWC} departs from the linear k_{TWC} vs. P_{stat} fit applied to all flight levels. A similar pattern is evident in SNOWIE 500 mb k_{LWC}. Possible causes of the unique 500 mb k_{TWC}/k_{LWC} behavior are explored in Section 2.3.3.

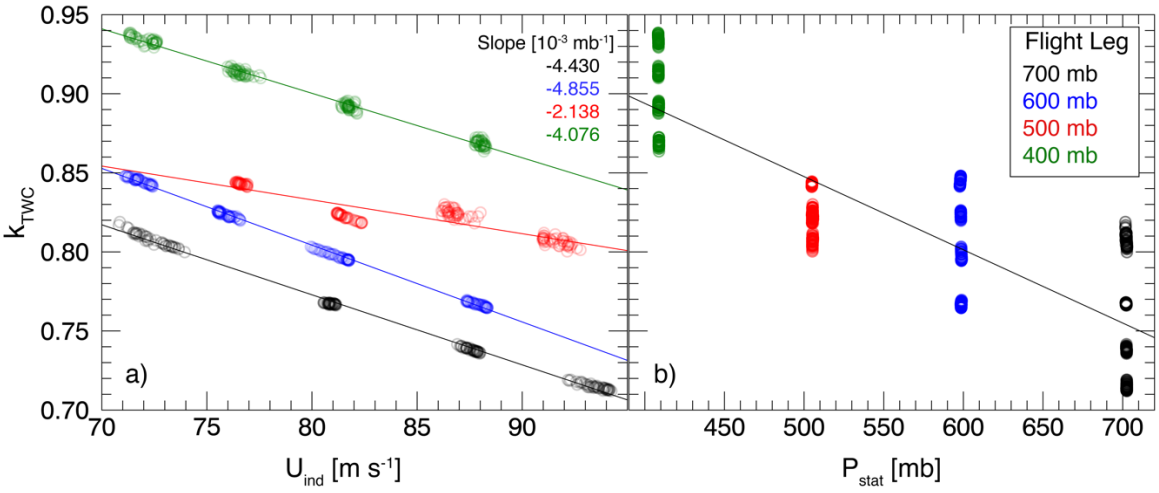

Figure 2.2 - *Scatterplots of SNOWIE k_{TWC} values plotted against a) U_{ind} and b) P_{stat}. Flight legs are color-coded by flight level. Lines in figure a) are linear k_{TWC} vs. U_{ind} fits applied on a per-flight*

level basis with slope values listed in the upper right corner. The black line in b) shows a linear regressions fit to k_{TWC} vs. P_{stat} for all 4 flight levels.

2.3.2 - An assessment of TWC k calibration performance

The following is an evaluation of the three k_{TWC} calibrations' performance utilizing data collected during calibration flights and 12 subsequent research flights. Residual TWC signal for clear air points is examined because it indicates the amount of uncertainty that k drift introduces in TWC measurements. Clear air data are selected from the 15 flights using the following criteria: *clear air data are those occurring in consecutive 2 second periods of 0 CDP counts and 0 Cloud Imaging Probe (CIP) counts.* Applying clear air criteria results in a subset of 35,471 clear air data that were collected for a range of airspeeds, static temperatures, and pressures. Clear air data have the following 5th – 95th percentile ranges; T: -28.52 – -1.71 C, P_{stat}: 408.88 – 702.28 mb, U_{true}: 85.05 – 119.60 m s^{-1}

Residual TWC signal for clear air points is calculated three separate times using k_{TWC} parameterizations from each calibration flight. The resulting values of residual TWC are employed as performance metrics.

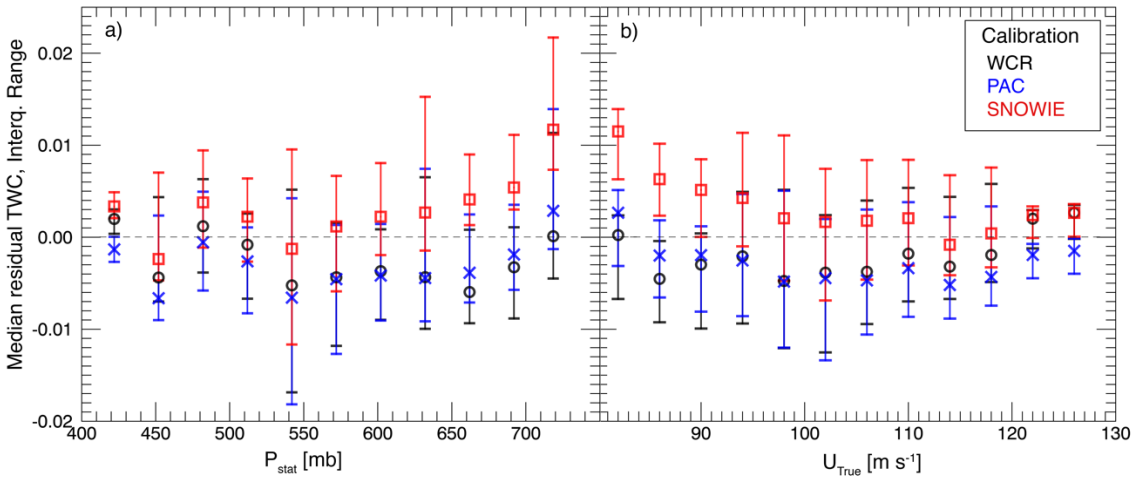

Figure 2.3 - *Median and interquartile residual TWC for all clear air data binned by a) P_{stat} and b) U_{true}. Colors denote k_{TWC} calibrations. Residual TWC is plotted against U_{true}, instead of U_{ind}, to better isolate residual TWC airspeed dependence.*

All calibrations produce residual TWC with little dependence on P_{stat} or U_{True}; as shown in Figure 2.3. Table 2.2 shows that all k_{TWC} fits produce absolute mean and median residual TWC less than 0.005 g m^{-3} and absolute standard deviation less than 0.018 g m^{-3}. Only the SNOWIE k_{TWC} fit produces a positive baseline offset and likewise has a 95th percentile residual TWC that is approximately twice as large as the other k_{TWC} fits.

Table 2.2 – *Mean, standard deviation, median, and 95th percentile residual TWC.*

Calibration	Mean residual TWC [g m^{-3}]	Median residual TWC [g m^{-3}]	95th %ile residual TWC [g m^{-3}]
WCR	-0.0031 ± 0.0159	-0.0033	0.0057
PAC	-0.0047 ± 0.0177	-0.0044	0.0073
SNOWIE	0.0030 ± 0.0158	0.0029	0.0133

2.3.3 – General $LWC\ k$ calibration characteristics

k_{LWC} calibrations have a less significant P_{stat} dependence than k_{TWC} calibrations. Coefficient values in Table 2.1 and Table 2.3 (showing values for k_{TWC} and k_{LWC} fits respectively) show that P_{stat} coefficients for k_{LWC} fits are an order of magnitude less.

Table 2.3 - *Coefficient values and goodness-of-fit statistics for each k_{LWC} fit. Same as Table 2.1 but for k_{LWC}, instead of k_{TWC} fits.*

Calibration	P_{stat} coef. (A) [mb^{-1}]	U_{ind} coef. (B) [m^{-1} s]	Intercept parameter (C)	r^2	Root Mean Squared Error
WCR	$1.51*10^{-5}$	$-2.92*10^{-3}$	1.97	0.9588	0.0052
PAC	$-7.61*10^{-5}$	$-1.97*10^{-3}$	1.89	0.9336	0.0052
SNOWIE	$9.91*10^{-5}$	$-3.76*10^{-3}$	1.97	0.7104	0.0170

The k_{LWC} WCR, PAC, and SNOWIE calibrations have a few distinct differences. SNOWIE k_{LWC} for the 500 mb flight level shows k_{LWC}, U_{ind}, and P_{stat} relationships that resemble SNOWIE 500 mb k_{TWC} relationships. The high variability in SNOWIE 500 mb k_{LWC} results in r^2 and RMSE that is twice that of WCR and PAC (see Table 2.3). Figure 2.4 illustrates the peculiar nature of SNOWIE 500 mb k_{LWC}.

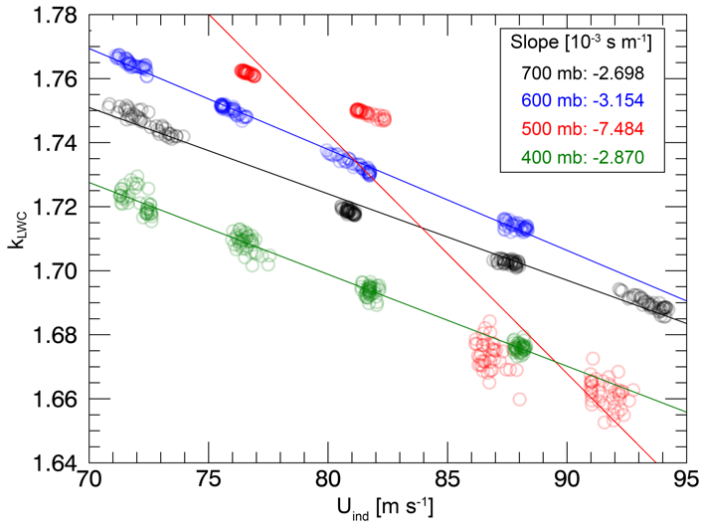

Figure 2.4 – *SNOWIE k_{LWC} plotted against U_{ind}. k_{LWC} values are color coded by flight leg level. Solid lines show linear fits applied on a per-flight level basis and linear fit slopes are inlaid (units are 10^{-3} / m s^{-1}).*

SNOWIE k_{LWC} for the two greatest 500 mb airspeed legs is much smaller than k_{LWC} for the lesser 500 mb airspeeds. Values inlaid in Figure 2.4 show that the slope of the 500 mb group is more than twice that of the other flight levels. It is not clear why both k_{LWC} and k_{TWC} (shown in Figure 2.4 and Figure 2.2) for the two higher 500 mb airspeed groups diverge from expected trends. Their unique behavior does not seem to be caused by variations in aircraft angle of attack, roll, or sideslip. It was also considered that the erratic behavior of 500 mb k_{LWC}/k_{TWC} could be due to radiative effects, but radiative heating is expected to be insignificant compared to sensible and latent heat losses. A correlation between k and aircraft heading could indicate that k is affected by radiative heating but no such correlation is present.

WCR and PAC 500 mb k_{LWC} (red in Figure 2.5) does not show the same erratic behavior as SNOWIE 500 mb k_{LWC} (Figure 2.4).

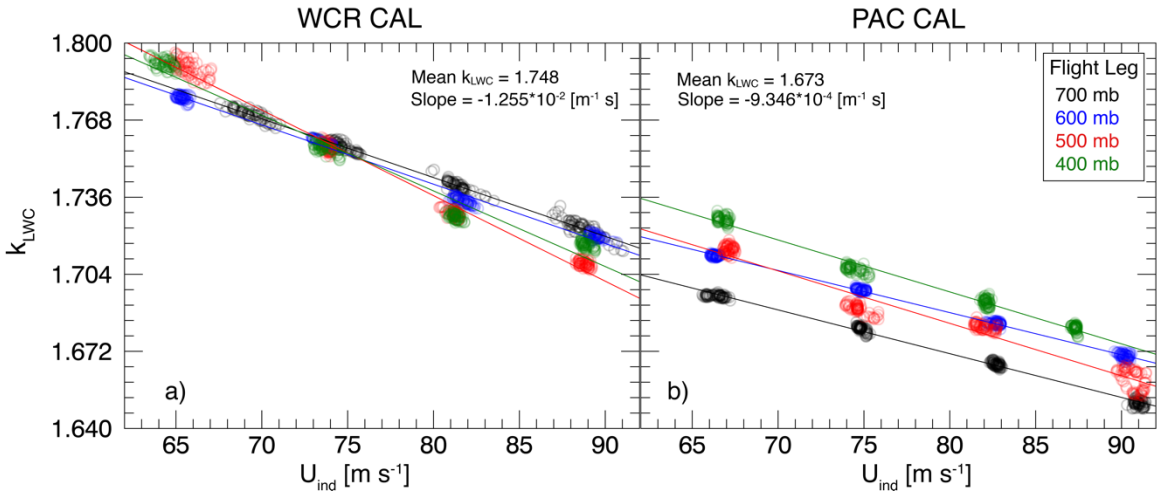

Figure 2.5 - *k_{LWC} vs. U_{ind} relationships for the WCR and PAC calibrations. Flight legs are color coded according to legend in b). Lines are linear fits applied to k_{LWC} on a per flight level basis. Slope values are from a linear fit to k_{LWC} collected at all flight levels.*

2.3.4 - An assessment of LWC k calibration performance

Table 2.4 shows that the WCR and PAC k_{LWC} fits produce absolute mean residual LWC less than 0.007 g m^{-3}. The PAC k_{LWC} fit is an outlier; it produces an absolute mean residual LWC that is approximately three times larger than the other calibrations. Standard deviation k_{LWC} is approximately 0.01 g m^{-3} for all calibrations but 95th percentile residual LWC ranges from approximately 0.01 – 0.04 g m^{-3}.

Table 2.4 – *Residual LWC statistics for each k_{LWC} calibration. Same as Table 2.2 but for* k_{LWC}*, instead of* k_{TWC}*, fits.*

Calibration	Mean residual LWC [g m^{-3}]	Median residual LWC [g m^{-3}]	95th %ile residual LWC [g m^{-3}]
WCR	-0.0008 ± 0.0096	-0.0005	0.0141
PAC	0.0225 ± 0.0110	0.0259	0.0354
SNOWIE	0.0066 ± 0.0105	0.0074	0.0228

Figure 2.6a shows that none of the k_{LWC} fits produce residual LWC with significant dependence on P_{stat}. Figure 2.6b indicates that residual LWC calculated with the PAC k_{LWC} fit is inversely related to U_{True}. The PAC k_{LWC} fit causes residual LWC overestimation of ~0.04 g m^{-3} at lower airspeeds. It is not surprising that the PAC k_{LWC} fit produces airspeed dependent residual LWC considering that it has the smallest U_{ind} coefficient (coefficient 'B' in Table 2.3).

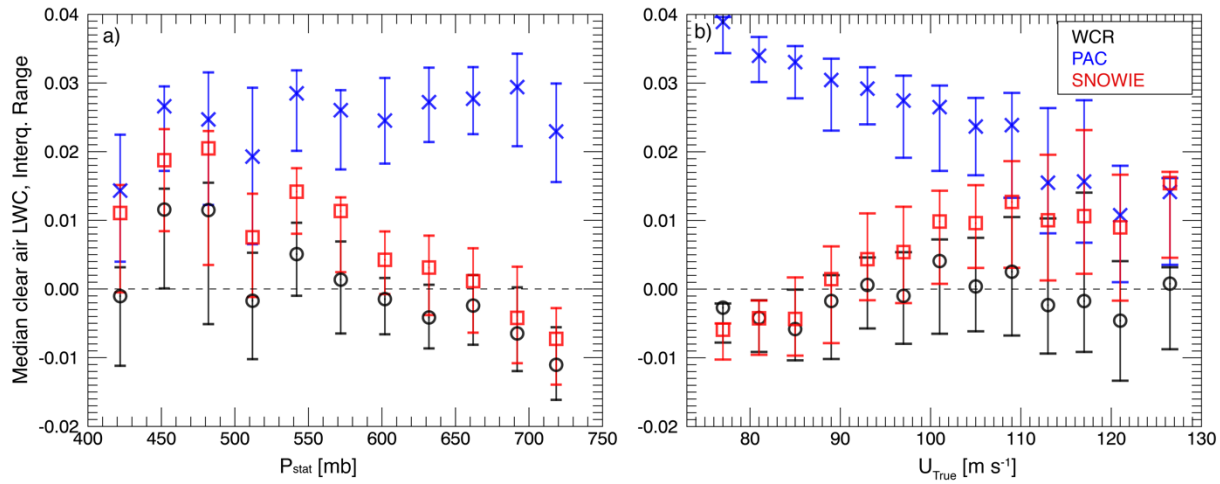

Figure 2.6 - *Median and interquartile residual LWC binned by a) P_{stat} and b) U_{true}.*

r^2 and RMSE for k_{LWC} fits do not necessarily correspond with k_{LWC} fit performance. Table 2.3 shows that the SNOWIE k_{LWC} fit has the smallest r^2 and RMSE that is three times greater than the other fits. Nonetheless, the SNOWIE fit produces the second smallest

95th percentile residual LWC and an absolute mean residual LWC that is approximately 30% of PAC fit mean residual LWC.

2.4 – Minimum detectable signal of TWC and LWC

The minimum detectable signal of TWC and LWC (MDS TWC, MDS LWC) are the minimum meaningful values of TWC/LWC. Stated in a different manner, MDS TWC and MDS LWC are TWC/LWC values just greater than what can be attributed to baseline drift and baseline noise. Since baseline drift is primarily caused by convective heat losses it follows that MDS TWC and MDS LWC are mostly dependent on the effectiveness of the k calibration method discussed above.

Table 2.5 – *Residual TWC and LWC statistics for each k_{LWC} calibration. Mean residual TWC/LWC, standard deviation residual TWC/LWC, and 95th percentile residual TWC/LWC for each calibration. Values are duplicates of those from Table 2.2 and Table 2.4.*

Calibration	Mean residual TWC [g m^{-3}]	95th %ile residual TWC [g m^{-3}]	Mean residual LWC [g m^{-3}]	95th %ile residual LWC [g m^{-3}]
WCR	-0.0031 ± 0.0159	0.0057	-0.0008 ± 0.0096	0.0141
PAC	-0.0047 ± 0.0177	0.0073	0.0225 ± 0.0110	0.0354
SNOWIE	0.0030 ± 0.0158	0.0133	0.0066 ± 0.0105	0.0228

MDS TWC and MDS LWC are evaluated using 95th percentile residual TWC and LWC. The three k_{TWC} calibrations produce similar 95th percentile residual TWC. It can be expected that MDS TWC is near 0.01 g m^{-3} (the mean of 95th percentile residual TWC from all calibrations). 0.01 g m^{-3} is equal to LWC that would be derived from approximately 2 cm^{-3} of 21 μm diameter droplets.

$MDS\ TWC$ calculated using our calibration method is an order of magnitude larger than Cotton et al.'s $MDS\ TWC$ (±0.001 g m^{-3}) (Cotton et al., 2013). Cotton et al.'s research focused on in-situ measurements of cirrus cloud. It is possible that their $MDS\ TWC$ is smaller because the researchers were operating in a narrower range of pressure and density (this is conjecture; the paper did not state operational flight levels). Cotton et al.'s $MDS\ TWC$ of ±0.001 g m^{-3} seems too optimistic given that it is less than the Nevzorov manual's stated baseline sensitivity of ±0.0015 g m^{-3} (SkyPhysTech). It is possible that the researchers' $MDS\ TWC$ is so small because their calculation method introduced another source of TWC bias. The formulas used to calculate TWC were not given so it is difficult to explore this notion.

The SNOWIE k_{LWC} fit is considered an outlier because it produces mean and 95th percentile residual LWC that is significantly greater than the other k_{LWC} fits. By taking the mean of WCR and SNOWIE 95th percentile LWC, $MDS\ LWC$ is shown to be approximately 0.02 g m^{-3} (the LWC that would be derived from a droplet population made of 4 cm^{-3} 21 μm droplets).

2.5 – Concluding remarks

The Nevzorov is a hotwire probe that provides measurements of LWC and TWC using the amount of energy required to maintain sensor temperature while cloud particles are impacted and evaporated. The Nevzorov features reference sensors to aid in the removal of convective heat losses. TWC and LWC calculations include a convective heat

loss coefficient (k) that is dependent on airspeed and density. In-flight changes of density and airspeed cause uncertainty in measurements of TWC and LWC.

A k calibration method that uses clear air data collected during calibration flights is presented. Three calibration flights were flown and linear parameterizations of k dependence on indicated airspeed and pressure are developed. The effectiveness of each calibration is examined using the residual signal of TWC and LWC for clear air points.

The k_{TWC} fits produce mean residual TWC that varies 0.006 g m^{-3}. k_{LWC} fits produce a larger range of mean residual LWC (0.023 g m^{-3}). PAC k_{LWC} is smaller than WCR or SNOWIE k_{LWC} and thus produces a larger mean residual LWC. It is unclear what causes PAC k_{LWC} to be smaller than WCR or SNOWIE k_{LWC}. A similar behavior is not observed in PAC k_{TWC}.

95th percentile residual TWC and LWC are used to estimate $MDS\ TWC$ and $MDS\ LWC$. The three k_{TWC} parameterizations produce 95th percentile residual TWC that varies less than 0.008 g m^{-3}. $MDS\ TWC$ is therefore calculated as the mean of 95th percentile residual TWC from all three k_{TWC} fits and equals 0.01 g m^{-3}.

PAC k_{LWC} is significantly smaller than WCR or SNOWIE k_{LWC} and produces mean residual LWC that is an order of magnitude greater than the other k_{LWC} fits. Therefore, the PAC k_{LWC} fit is considered an outlier and is not used to evaluate $MDS\ LWC$. 95th

percentile residual LWC calculated using the WCR and SNOWIE k_{LWC} fits predict that $\mathrm{MDS\ LWC}$ is approximately 0.02 g m^{-3}.

Chapter 4 will explore sources of Nevzorov uncertainty beyond convective heat losses. It will also present examples of Nevzorov measurements made in different cloud phases and environmental conditions. Comparisons between Nevzorov LWC and CDP LWC are also presented.

3 - A droplet generating calibration device to investigate CDP uncertainty

3.1 CDP operating principles

The CDP is a forward scattering optical particle counter (OPC) that is commonly used to research cloud processes. It is capable of sizing and counting droplets ranging from 2 – 50 μm in diameter from which Droplet Size Distributions (DSDs) can be computed. DSDs can be used to derive several parameters including droplet concentration, mean diameter, effective diameter, and measurements of LWC (Droplet Measurement Technologies, 2014).

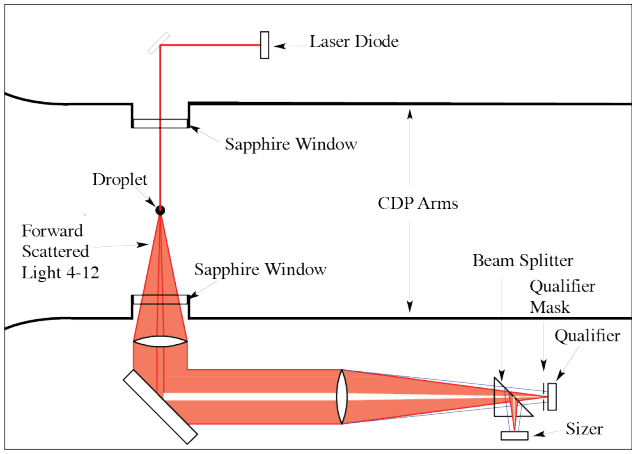

Figure 3.1 - *A top-down CDP schematic showing the general arrangement of the laser, collecting optics, and the sizer and qualifier photodetectors. The tips of the probe arms are pointing to the left (out of frame). The droplet (small black circle scattering laser light) would be travelling left to right. Adapted from work by Lance, et al. (2010).*

The CDP measures droplet properties using an open path laser that is passed between the arms of the probe, a series of collecting optics, and two photodetectors. Figure 3.1 shows the approximate location of these components. As droplets pass between the

probe arms, some intersect the laser and scatter energy. Photons are collected and focused onto a mirror with a hole in its center called the “dump spot”. The dump spot excludes unscattered high intensity light that is capable of damaging components. The remaining light is focused onto a beam splitter which passes some of the light to a ‘sizer’ and the remaining light to a ‘qualifier’ photodetector (Droplet Measurement Technologies, 2014). Cloud droplets are spherical and have a know index of refraction. Therefor Mie-Lorenz theory and sizer detector voltage responses (directly related to the intensity of forward scattered light) can be used to estimate droplet size.

The qualifier detector is covered by a rectangular mask so that it is only sensitive to photons scattered from a specific region of the laser beam; called the sample area. Light scattered from beyond the sample area is too diffuse to cause appreciable qualifier response (Droplet Measurement Technologies, 2014). To determine if a droplet is within the sample area, the qualifier response is doubled (“normalized qualifier response”) and compared to the sizer response. A droplet is considered to be within the sample area, and is subsequently sized and counted, if the normalized qualifier response is greater than the sizer response (Lance et al., 2010).

The sample area is constrained to a small region of the laser beam (work in 2010 by Lance et al. found sample area to measure as approximately 1400 x 200 μm) to help ensure that droplets both pass through regions of uniform laser intensity and have similar scattering angles. Inhomogeneity in laser beam intensity and variations of scattering angle can affect the amount of light that reaches the collecting optics and

thus contribute to sizing error. It is also important that the extent of the sample area is clearly defined because its dimensions are used in calculations of higher DSD moments.

The CDP operates on principles similar to the Forward Scattering Spectrometer Probe (FSSP) but incorporates several improvements including an updated qualifier detector to more clearly define sample area dimensions, a unimodal laser to produce a more homogenous laser beam, and an open-path design (opposed to the FSSP's cylindrical inlet) to decrease particle shattering bias (Baumgardner et al., 1985; Lance et al., 2010). Perhaps most importantly, the CDP features faster electronics (with a 40MHz clock speed) which effectively eliminates the deadtime loss errors that compromise FSSP measurements (Droplet Measurement Technologies, 2014). Baumgardner et al. (1985) estimated that deadtime losses in the FSSP cause a 10 - 20% undercounting bias at measured concentrations of 180 cm^{-3} and 400 cm^{-3} respectively.

3.2 – Possible sources of uncertainty in CDP measurements and DSD derived variables

Despite the mentioned improvements, the CDP is still subject to sizing and counting error caused by factors that alter the amount of laser energy reaching the collecting optics. Such factors include droplets passing through sample area regions of non-uniform laser intensity, droplets passing through regions beyond the intended sample area (which alters scattering angles), and misalignment of optical components (Lance et al., 2010).

Miscounting causes a scaling bias in droplet concentration and LWC. It can also cause artificial broadening of DSDs. Broadening can mistakenly be attributed to distribution-modifying cloud processes such as coalescent growth and entrainment/mixing. Missizing impacts the accuracy of parameters derived by DSD integration including Mean Diameter, Effective Diameter (the integrated 3rd moment divided by the 2nd moment), Volume-weighted Mean Diameter (or VMD; equal to the 4th moment over the 3rd), and derived LWC (Zender, 2002). Sizing error can especially impact LWC accuracy because errors in LWC scale as the 3rd power of error in droplet size.

Uncertainty in sample area dimension (SA) is a third factor that can contribute to uncertainty in CDP measurements. The dimensions of the sample area are used in sample volume calculations (where sample volume is simply sample area multiplied by true airspeed) meaning that errors in sample area bias higher moment calculations including concentration and LWC (Nagel et al., 2007).

Coincidence error is a concentration-dependent phenomenon that occurs when two or more droplets are simultaneously within the sample area. Coincident droplets register as a single counting event (by the CDP's design) resulting in undercounting. Coincident droplets are also capable of scattering additional light into the collecting optics and can therefore contribute to oversizing. Coincidence error will not be discussed in the remainder of chapter 3 but will be further explored in chapter 4. Chapter 3 will focus on

a calibration technique used to characterize uncertainty caused by factors other than coincidence.

In principle, a lab-based calibration could be used to assess non-coincident counting and sizing error, and obtain measurements of sample area dimensions. However, traditional CDP calibration methods (that utilize glass microbeads or polystyrene latex spheres (PSLs)) are ill-suited for such tasks. Using microbeads or PSLs to assess sizing performance is problematic because calibration particles often deviate from sphericity, have different refractive indexes than water, and have an associated degree of size uncertainty (Lance et al., 2010). It is also not possible to investigate the locational-dependence of sizing error or measure sample area with traditional calibration methods because they incorporate crude methods of placement control. Likewise, it is not possible to test counting accuracy because the concentration of calibration particles being passed through the sample area is unknown.

3.3 – A droplet generating calibration device

Lance et al. (2010, 2012) built a CDP calibration system that uses pure water droplets and a micro-positioning apparatus to circumvent the limitations of microbead and PSL-based calibrations. The device was mainly based on FSSP and Optical Array Probe (OAP) calibration systems developed by Nagel et al. (2007), Wendisch et al. (1996), and Korolev et al. (1991). The apparatus used piezoelectric printheads to create a stream of monodisperse water droplets that were subsequently accelerated by a sheath airflow and passed through the sample area of the CDP. Manual micro-positioning

stages controlled the point of droplet injection so that sizing and counting accuracy could be tested at discrete locations within the sample area and measurements of sample area dimensions could be obtained. The setup also provided an independent verification of droplet size using a high speed camera and the “Glare” technique (see last part of Section 3.3.1), as described in Korolev et al. (1991).

A droplet generating calibration system similar to Lance et al.’s design was developed at the University of Wyoming (UW). The setup was initially designed to evaluate and calibrate the University of Wyoming King Air (UWKA) CDP but could be modified for use with the FSSP and 2D-S OAP probes. The UW design differs from Lance et al.’s in that it uses computerized micro-positioning stages (vs. manual stages) to allow for autonomous operation and calibrations of finer spatial resolution.

3.3.1 – Main calibration system components

Printhead

Droplets are created using MicroFab Technologies piezoelectric printheads (model numbers: MJ-AT-01, MJ-ATP-01) that are used for a range of applications including circuit board fabrication and bio-medical engineering (MicroFab Tech., “Low Temperature Dispensing Devices”). Item A II in Figure 3.2a shows a schematic of a printhead with major components labeled. The printhead’s main body contains a cavity surrounded with a piezoelectric membrane that is excited by voltage pulses generated by a MicroFab JetDrive III printhead controller (green device in sub-system A IIX)

(MicroFab Tech., “JetDrive III”). The intensity and timing of pulse waveforms and droplet creation frequency are software adjustable. Printheads are available in orifice sizes ranging from 10 – 80 µm at 5 µm increments. Figures 3.3b and 3.3c show images of droplets being created at 10X and 1X magnifications.

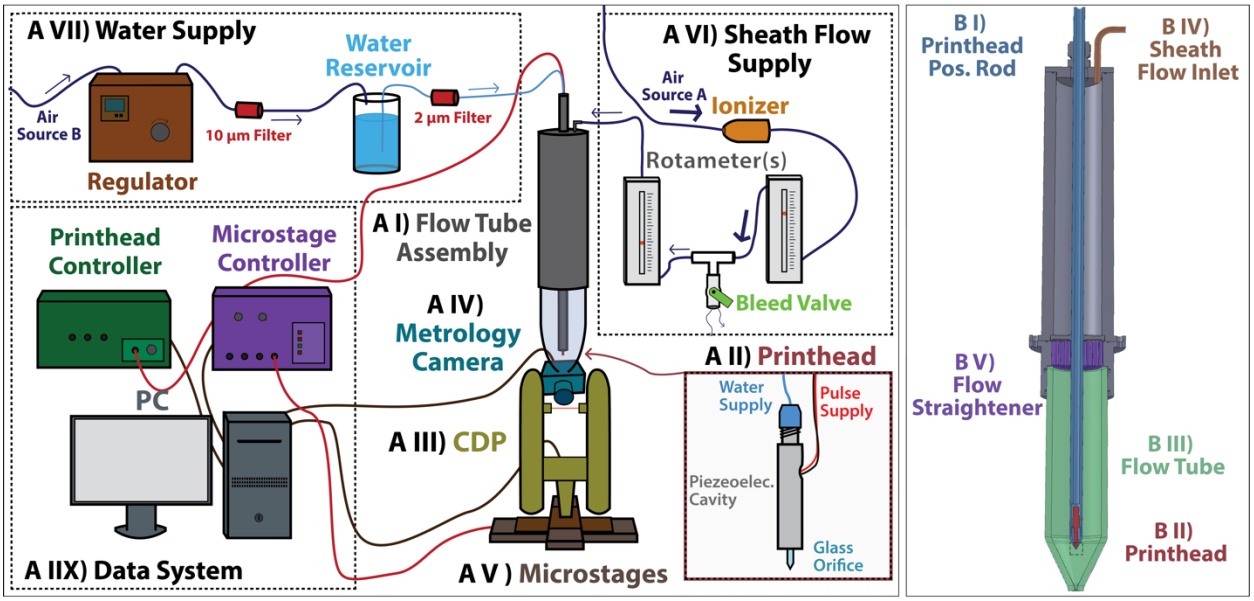

Figure 3.2 - *a) Major calibration system components. Groups of system subsets are outlined in dashed borders. Air lines are shown in purple, water: blue, red: outgoing communication, brown: incoming communication. b) Cutaway of the flow tube assembly (also shown as A I in Figure 3.2a).*

Water supply subassembly

The water supply subassembly (item A VII in Figure 3.2a) provides sub-micron filtered water to the printhead. A MicroFab CP-01 pressure regulator (MicroFab Tech., “Pneumatics & Temperature Controllers”) is used to supply precise amounts of pressure to a sealed water reservoir. The regulator can be adjusted to provide near-neutral pressure required for printhead operation, higher pressures used to purge water lines of

air bubbles, or a vacuum used to clean and de-clog printheads. A pair of inline filters on the air and water lines remove contaminants that could lead to printhead clogging.

Flow tube assembly

The flow tube assembly (shown as item A I in Figure 3.2a and as a cutaway view in Figure 3.2b) houses the printhead within a background sheath flow. Pressurized air enters the top of the assembly through the sheath flow inlet (B IV), passes through the flow tube's aluminum body, is made laminar by the honeycomb-style flow straightener (B V), and finally passes through and exits a glass flow tube (B III). The flow straightener's metal honeycomb design is a departure from the "sponge" style straightener used by Lance et al. in an effort to reduce sheath flow turbulence. The flow tube's tapered exit region accelerates sheath flow (and by extension droplets) and focuses droplets into a precisely-placed stream (Figure 3.3c shows an example of such a droplet stream). The printhead is secured at the end of an adjustable positioning rod (B I) allowing it to be positioned at any height within the flow tube. Changing printhead height allows for fine scale adjustment of droplet size by altering the degree of in-flow evaporation. The flow tube's exit region is positioned at discrete locations directly above the CDP's laser to minimize droplet deviation caused by turbulence (the distance between the flow tube and laser is exaggerated in Figure 3.2a; typical distances are approximately 3 mm or less).

Sheath flow supply subassembly

The sheath flow supply subassembly (Item A VI in Figure 3.2a) provides pressurized air to the flow tube assembly. Electro-static interactions between droplets and the flow tube can prevent droplets from successfully exiting the apparatus so a Simco-Ion 6110 ionizer (orange device in A VI) is placed in-line to neutralize static charge in the sheath flow supply (Simco-Ion, 2013). The ionizer requires greater flow volume than does the sheath flow (56 l min^{-1} vs. 13 l min^{-1}) so a bleed valve (lime green in A VI) is used to reduce flow volume prior to entering the flow tube assembly. A pair of rotameter flow meters placed on either side of the bleed value are used to ensure that proper flow volume is provided to both the ionizer and flow tube assembly.

Microstages

The CDP is secured atop two perpendicularly stacked ThorLabs LNR50S linear microstages (brown devices at the bottom of Figure 3.2a). The stages allow for 50 mm of movement in both the X/Y axes and are accurate to 1 μm (ThorLabs, Linear Translation Stages). A ThorLabs BSC201 microstage controller (shown in purple in Figure 3.2a) provides power and allows 2-way communication between the PC and microstages (ThorLabs, “APT Stepper Motor Controllers”). ThorLabs Kinesis software is used to manually and/or autonomously control stage position.

Metrology camera and the glare technique

A JAI CV-A10 CL high-speed metrology camera (Item A IV in Figure 3.2a) and an attached 10X microscope objective lens provide an independent measurement of

droplet size, velocity, and position (JAI, 2017). Measurements of droplet characteristics are obtained using the "Glare" technique, as described by Korolev et al. (1991), where images are taken of two bright regions at the left and right sides of droplets. These bright regions are caused by refraction of light through the droplets as they pass through the CDP's laser and appear as two bright parallel streaks (see Figure 3.3a below).

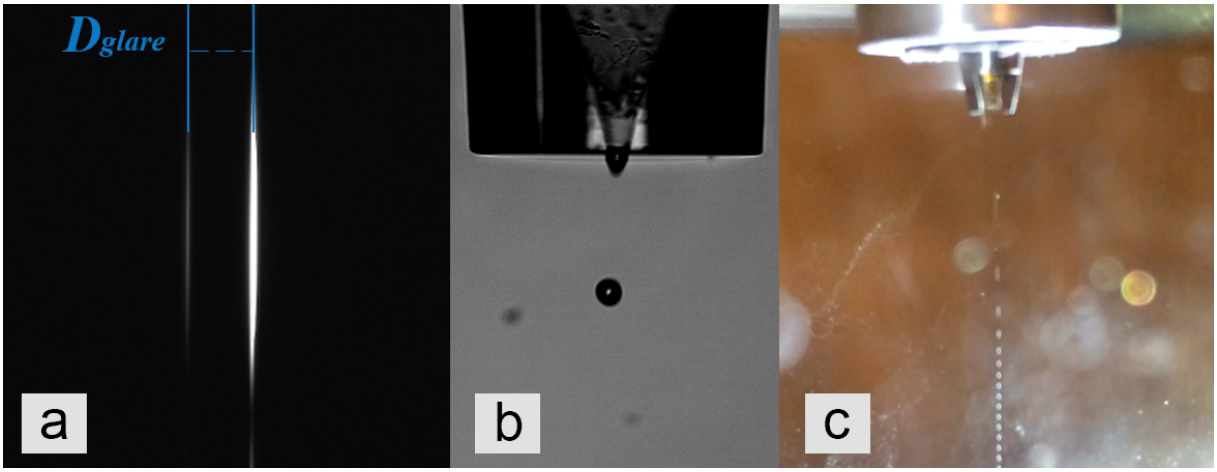

Figure 3.3 - *a) Glare streaks captured at 1/1000 sec with blue lines denoting the location of glare centerlines. b) 10X magnified image of a droplet being ejected from the printhead orifice. Note the miniscus protruding from the orifice exit. c) Printhead creating droplets inside the flow tube. The droplet stream was frozen with a strobe flashlight.*

Droplet size is calculated using the pixel distance between glare centerlines (manually measured in Adobe Photoshop), a pixel to distance conversion factor (found using a microscope calibration slide), and the following equation from Korolev et al. (1991).

$$D_{true} = \frac{2 * (D_{glare} * P)}{\frac{n * cos(2\gamma)}{[1 + n^2 - 2n * \sin(\gamma)]^{1/2}} + \sin(\gamma)} \quad (3.1)$$

where $Dtrue$ is droplet diameter, D_{glare} is the pixel distance between glare centerlines, P is a pixel to linear distance conversion factor (0.710 μm px^{-1}), n is the refractive index of water for the CDP's 0.658 μm wavelength laser (1.331), and $\boldsymbol{\gamma}$ is the angle between the camera objective and the laser's incident plane.

Errors in the measurement of $\boldsymbol{\gamma}$ introduce negligible uncertainty because D_{true} is relatively insensitive to $\boldsymbol{\gamma}$ for angles between 120 – 130º. A digital protractor was used to set $\boldsymbol{\gamma}$ to 125º using the side of the camera objective lens and the CDP's arm strut (shown as the rectangular structure connecting CDP arms in Figure 3.2a) as references. Limitations of protractor accuracy (±0.3º) equate to only $1.3*10^{-4}$ μm uncertainty in D_{true}. Other errors in $\boldsymbol{\gamma}$ measurement (such as operator measurement error) are unlikely to result in significant errors in droplet sizing. For example, a 3º departure from $\boldsymbol{\gamma}$ of 125º results in D_{true} error of less than 0.01 μm. All factors considered, expected uncertainty of D_{true} is ±0.355 μm, limited almost entirely by camera resolution.

Droplet position (normalized to the left edge of the image) is calculated using the longitudinal position of the dimmest glare's centerline and P. Position is likewise accurate to ±0.355 μm.

Droplet velocity is estimated by capturing images using short exposure length (1/150,000 – 1/300,000 sec) resulting in glare streaks with well-defined start and end points. Glare length, P, and exposure time can then be used to provide estimates of droplet velocity accurate to within ±0.10 m s^{-1}.

3.3.2 – Droplet creation requirements

In order to investigate sizing and counting error, the calibration system must meet four droplet production requirements. The calibration system must be capable of producing a range of droplet sizes (ideally 3 – 49 µm) in order to evaluate how droplet size affects sizing and counting. Droplet size may be altered using two methods. Size can be either coarsely-adjusted using printheads of different orifice size (printheads with 15, 20, 25, 30, 35, and 40 µm orifices were available for this work) or finely-adjusted by altering printhead height within the flow tube which affects in-flow residence time (and by extension, the amount of in-flow evaporation). Table 3.1 tabulates statistics for seven calibration runs. For each run, the table shows, the mean, standard deviation, and 95th – 5th percentile range for $\mathrm{D_{true}}$. The seven calibration runs produced droplets with mean diameter of 9, 17, 24, 29, 34, 38, and 46 µm. Throughout the runs, standard deviation in the true droplet diameters varied by no more than 0.66 µm, and 90% of all drops in a single run were generally within 2 µm diameter. Note that the printheads create droplets that are 30 – 50% larger than their orifice size; which allowed a 40 µm printhead to create 46 µm droplets.

The system must be capable of producing droplets of consistent size throughout a calibration run, which typically takes around 3.5 hours to complete. It is difficult to produce droplets smaller than 15 μm for extended periods because printheads with smaller orifices are more sensitive to fluctuations in water supply pressure. Hence, the 9 μm calibration was shorter in duration than the 17 – 46 μm calibrations.

Table 3.1 - *D_{true} size distribution statistics for seven calibrations. Calibration name, duration, and D_{true} mean, standard deviation, and 95th – 5th percentile ranges for $\mathrm{D_{true}}$ calculated from 80 randomly selected glares.*

Calibration	Duration [hour]	Mean $\mathrm{D_{true}}$ [μm]	$\mathrm{D_{true}}$ 95th – 5th %ile range [μm]
9 μm	1.71	8.975 ± 0.486	1.547
17 μm	3.23	17.322 ± 0.529	1.547
24 μm	4.62	24.440 ± 0.421	0.774
29 μm	4.35	28.753 ± 0.660	2.321
34 μm	3.95	33.599 ± 0.404	0.774
38 μm	3.58	38.463 ± 0.352	0.774
46 μm	4.74	46.026 ± 0.408	0.774

Table 3.1 shows calibration duration, and $\mathrm{D_{true}}$ statistic for a sample of 80 randomly selected glares. $\mathrm{D_{true}}$ 95th – 5th percentile ranges (last column) indicate that the system was capable of producing droplets of consistent size throughout each calibration run (a majority of which lasted 3 – 5 hours). Half of the calibrations had a $\mathrm{D_{true}}$ 95th – 5th percentile range of 0.774; most of this variation can be attributed to camera resolution limitations which introduce ±0.355 μm uncertainty in $\mathrm{D_{true}}$. The largest 95th – 5th percentile $\mathrm{D_{true}}$ range (2.321 μm) was marginally greater than the CDP's 2 μm bin resolution for the 14 – 50 μm bins. The standard deviation of $\mathrm{D_{true}}$ is approximately 0.4 μm for half of the calibrations and less than 0.6 μm for all but the 29 μm calibration.

Droplets must be consistently placed within a 10 x 10 μm wide region (the finest spatial resolution used) for the duration of a calibration run. Two tests were used to confirm droplet placement repeatability. For the first test, glare images were captured from two perpendicular angles (124.9 and 214.9º incident to the CDP's laser) over the course of one hour to confirm that placement repeatability was similar along orthogonal axes. In the second placement test, glares were captured during a four-hour period with the camera at 124.9º incident to the CDP's laser in order to validate long-term droplet placement repeatability. Both tests used ~32 μm diameter droplets, an intermediate printhead height, and sheath flow of 13 l min^{-1}.

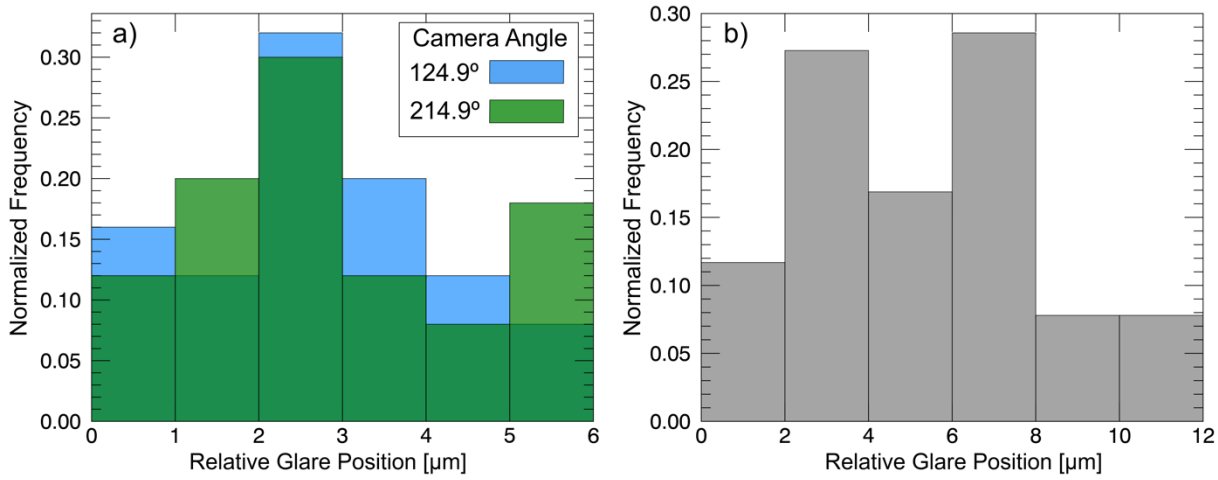

Figure 3.4 - *Relative glare positions (glare position – minimum glare position) for a) One-hour test with camera placed at perpendicular angles. Blue bars are for positions of glares taken at 124.9º incident and green for images captured at 214.9º incident. b) Relative glare positions for the four-hour test. Distributions were calculated from random samples of 50 glares for each camera angle in the one-hour test and 80 random glares for the four-hour test.*

Figure 3.4 shows distributions of relative glare position (relative position = position – minimum position) for the one and four hour tests. Both the 124.9º and 214.9º camera

angles for the one-hour test resulted in similar positional repeatability. Relative positions from both camera angles had an absolute range of 5.714 μm and respective standard deviations of 1.470 and 1.663 μm. Relative positions from the four-hour test show that approximately 87% of droplets were placed at positions between 2 and 8 μm. Overall, relative glare position had an absolute range of 11.429 μm, had a 95^{th} – 5^{th} percentile range of 9.286 μm, with a standard deviation of 2.848 μm. The absolute range of droplet position indicates that approximately 8% of droplets were placed beyond 10 μm; a factor that is taken into consideration while analyzing and presenting calibration results.

The system must be able to eject droplets at velocities greater than the CDP's minimum operational airspeed of 10 m s^{-1} (Droplet Measurement Technologies, 2014). Flow measurements taken at the flow tube exit indicate that sheath flow velocity is ~32 m s^{-1} at the exit region. A sample of 30 glare streaks (with exposure times of 1/150000 sec) captured during the four-hour droplet placement test were used to estimate droplet velocity with an input flow of 13 l min^{-1}. The sample had a mean velocity of 33.2 m s^{-1}. An input flow of 13 l min^{-1} was deemed appropriate for calibrations of all droplet sizes so long as the printhead is placed at heights above the beginning of the flow tube's tapered exit region (it is assumed that all appreciable sheath flow acceleration occurs in the tapered exit region). It can also be assumed that a flow of 13 l min^{-1} is sufficient for all droplet sizes because differences in droplet mass will negligibly affect exit velocity.

3.3.3 – Calibration procedure

When preparing for a calibration, the glass flow tube is first removed so that printhead operation can be closely observed. The regulator (brown box in Figure 3.2a) is set to apply high air pressure to the water reservoir which forces water through the printhead orifice and creates a steady “purge stream”. Purging removes air bubbles in water supply lines and is used to visually confirm that the printhead is clear of obstructions. A purge stream from a clogged printhead will eject at an angle, split into multiple streams, or will simply be absent. If the printhead appears to be clogged it is removed from the printhead positioning rod and cleared using an ultrasonic cleaner and back-flushing as described in MicroFab Inc., “MicroJet Cleaning Guide”.

Once the printhead successfully produces a steady purge stream, the printhead controller is activated to apply voltage pulses to the printhead’s piezoelectric cavity and the regulator is adjusted to apply near-neutral pressure to the water reservoir. The printhead will begin to produce a stream of droplets that are inspected to confirm that only a single droplet is being ejected at a time. Additional or “satellite” droplets are evident as multiple smaller droplet streams. If necessary, the printhead controller waveform is adjusted to eliminate satellite droplets.

Next, the flow tube is replaced and wiped with Static Guard to neutralize charge introduced by handling. The sheath flow is adjusted to 13 l min^{-1} and the microstages are repositioned so that droplets are passed through the CDP’s laser. An estimate of

droplet size is obtained from a sample of glare images and if necessary, printhead height is adjusted to produce droplets of the desired size.

After it is confirmed that suitably-sized droplets are being created, sample area bounds are found by repositioning the CDP while monitoring its output. Bounds are defined as the position where accepted droplet counts go to 0. A script is programmed to alter CDP position so that droplets are placed at set spatial intervals that cover the entire sample area. The script moves the microstages so that droplets are placed at each sample location for a set amount of time (typically 1 to 2 seconds) and then alters the droplet injection point by repositioning the stages by a specified amount (typically 10, 20, or 30 μm). The sequence is repeated to “walk” the droplet injection point across the entire sample area in a serpentine pattern.

After programming the microstage script, the metrology camera is set to capture 60 glares every 30 seconds in order to provide a large sample of glares for analysis, CDP software is activated to record measurements to a csv file every 0.25 second, and the calibration is initiated by starting the microstage script.

Upon completion of the calibration run, the CDP, printhead, and sheath flow are deactivated. The CDP csv file and a diagnostic log output by the microstage software are read into IDL and times are synchronized to give CDP responses specific to each sample location. CDP measurements that were recorded while the microstages were in motion are omitted so that only data recorded at each sample interval are considered.

Finally, 80 randomly-sampled glares are analyzed to provide an estimate of "true" droplet size (as described in the *Metrology Camera and the Glare Technique* subsection in Section 3.3.1).

3.4 – Calibration results

Seven calibrations that tested CDP response at set intervals across the entire sample area were conducted using 9, 17, 24, 29, 34, 38, and 46 μm droplets. Table 3.2 shows the number of droplets created per sample location and sample location longitudinal/latitudinal resolution for each calibration.

Table 3.2 - *Calibration characteristics and statistics of D_{true}* and D_{CDP} distributions. Calibration name, the number of droplets placed at each sample location, sample location longitudinal and latitudinal resolution, and median, mean, and standard deviation of D_{true}* and D_{CDP}. D_{true}* is equal to D_{true} rounded to the geometric mean of each CDP's size bin. D_{true}* statistics were calculated from 80 random glares. D_{CDP} statistics are from CDP responses recorded during the entirety of each calibration.*

Calibration	Droplets per sample location	Long. Res. [μm]	Lat. Res. [μm]	Median D_{true}* [μm]	Mean D_{true}* [μm]	Median D_{CDP} [μm]	Mean D_{CDP} [μm]
9 μm	200	30	20	9.5	9.100 ± 0.628	7.5	7.794 ± 0.658
17 μm	250	10	10	17.0	17.025 ± 0.389	17.0	17.444 ± 0.990
24 μm	500	10	10	25.0	24.175 ± 0.991	25.0	23.873 ± 2.395
29 μm	500	10	10	29.0	28.625 ± 1.011	31.0	29.397 ± 3.171
34 μm	500	10	10	33.0	33.825 ± 0.991	35.0	33.694 ± 4.170
38 μm	500	10	10	39.0	38.425 ± 0.911	41.0	38.601 ± 4.708
46 μm	500	10	10	45.0	46.950 ± 1.005	49.0	45.855 ± 6.557

All but one of the calibration runs used a spatial resolution of 10 μm x 10 μm. The 9 μm calibration used a coarser resolution (30 μm x 20 μm) because small droplets were

more difficult to produce for extended periods and the coarser resolution allowed completion of the run in significantly less time. Calibrations were conducted with three different droplet counts per location; 200 droplets (9 μm calibration), 250 droplets (17 μm calibration), or 500 droplets (24, 29, 34, 38, and 46 μm calibrations).

Our experimental design differs from Lance et al.'s 2010 work in two main manners. Lance et al. conducted two "full" calibrations that used 12 and 24 μm droplets to test CDP sizing and counting accuracy throughout the entire sample area and provide measurements of sample area dimensions. The researchers then conducted nine additional calibrations using 8 – 36 μm droplets that only tested sizing and counting accuracy in the center of the sample area. In contrast, we conducted seven full calibrations using 9 – 46 μm droplets. Our tests typically used spatial resolutions of 10 x 10 μm whereas Lance et al.'s were conducted with a 200 x 20 μm resolution. Completing seven full calibrations with finer spatial resolution provides more accurate measurements of sample area across the range of detectable droplet sizes.

3.4.1 - Droplet sizing performance

The last four columns in Table 3.2 show median, mean, and standard deviation of D_{CDP} (CDP binned counts rounded to the geometric mean of each bin) and D_{true}* (D_{true} rounded to the geometric mean of the CDP size bin they fall within). D_{true}*, instead of simply D_{true}, is used because it considers the affects of missizing, miscounting, and error in SA but still accounts for uncertainty due to limitations of CDP size bin resolution.

Figure 3.5 shows distributions of D_{true}* and D_{CDP}. Table 3.2 and Figure 3.5 illustrate a few important points regarding CDP sizing accuracy and precision.

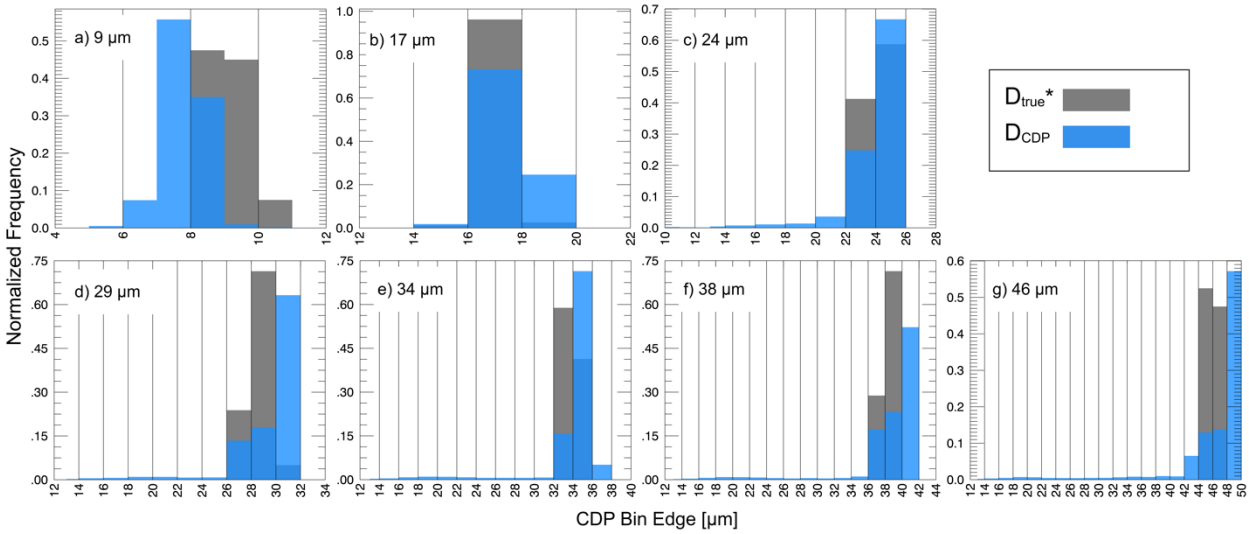

Figure 3.5 - *Distributions of D_{true}* (grey) and D_{CDP} (blue) for each calibration (as designated in the upper left corner of each plot). D_{true}* distributions are calculated from 80 random glares. D_{CDP} distributions are from all CDP responses recorded during the calibration.*

CDP sizing accuracy is not directly related to droplet size. For most calibrations, the absolute difference of mean D_{true}* and mean D_{CDP} is less than 1 µm. For the 9 and 46 µm calibrations' mean D_{true}* vs. mean D_{CDP} differences were slightly greater but remain less than 1.5 µm.

In contrast, CDP sizing precision is a function of droplet size. The standard deviation of D_{CDP} (in Table 3.2) show that D_{CDP} spectral width increases with increasing droplet diameter. This relationship is a direct result of the measurement from the CDP since there appear no similar broadening of D_{true}*.

For D_{true} larger than 17 μm, the CDP has a tendency to undersize approximately 5 – 10% of droplets by 20 – 30 μm resulting in tails of the measured (D_{CDP}) distribution extending towards smaller sizes. This is especially noticeable in Figures 3.5 c, d, e, f, and g (those calibrations conducted with droplet diameters 24 μm and larger).

The CDP tends to skew droplet spectra toward larger size. The difference of median D_{CDP} and mean D_{CDP} (in Table 3.2) shows that skewedness becomes more pronounced as droplet size increases; the 9 and 17 μm calibrations have median D_{CDP} vs. mean D_{CDP} differences of -0.294 μm and -0.444 μm while the 38 and 46 μm calibrations have median D_{CDP} vs. mean D_{CDP} differences of 2.399 μm and 3.145 μm. Figure 3.5 shows this behavior is most apparent for the calibrations of 29 μm and larger.

Figure 3.6 displays "beam maps" which are two-dimensional representations of the locationally-dependent CDP response as observed from the top of the sample area. These maps show the difference of D_{CDP} and mean D_{true}* as a function of the two dimensional location within the sample area. The beam maps show that the sample area is elliptical, occupies 1500 – 1600 μm of the beam's length, and covers ~200 μm of the beam's width.

Droplets are greatly undersized at the far-right side of the sample area (side nearest detector) for droplets larger than 17 μm. These regions of severe under sizing can account for the leftward D_{CDP} tails evident in Figure 3.5. It is possible that this behavior occurs because droplets close to the collecting optics have smaller scattering angles

and tend to scatter the most energy in angles that are masked by the dump spot. This decreases the intensity of light reaching the sizer and causes droplets to be undersized. Droplets greater than 17 µm that pass through this 'undersizing region' must also scatter enough light through the qualifier mask to cause normalized qualifier signal to exceed the sizer signal. A relatively small qualifier response would be sufficient to qualify droplets passing through the sample area's right side because sizer response is likewise small. The size of the undersizing region on the right side of the sample area is directly related to droplet size. This behavior may result from the fact that larger droplets scatter in greater angles and are therefor more likely to scatter energy into the collecting optics when transiting near sample area bounds.

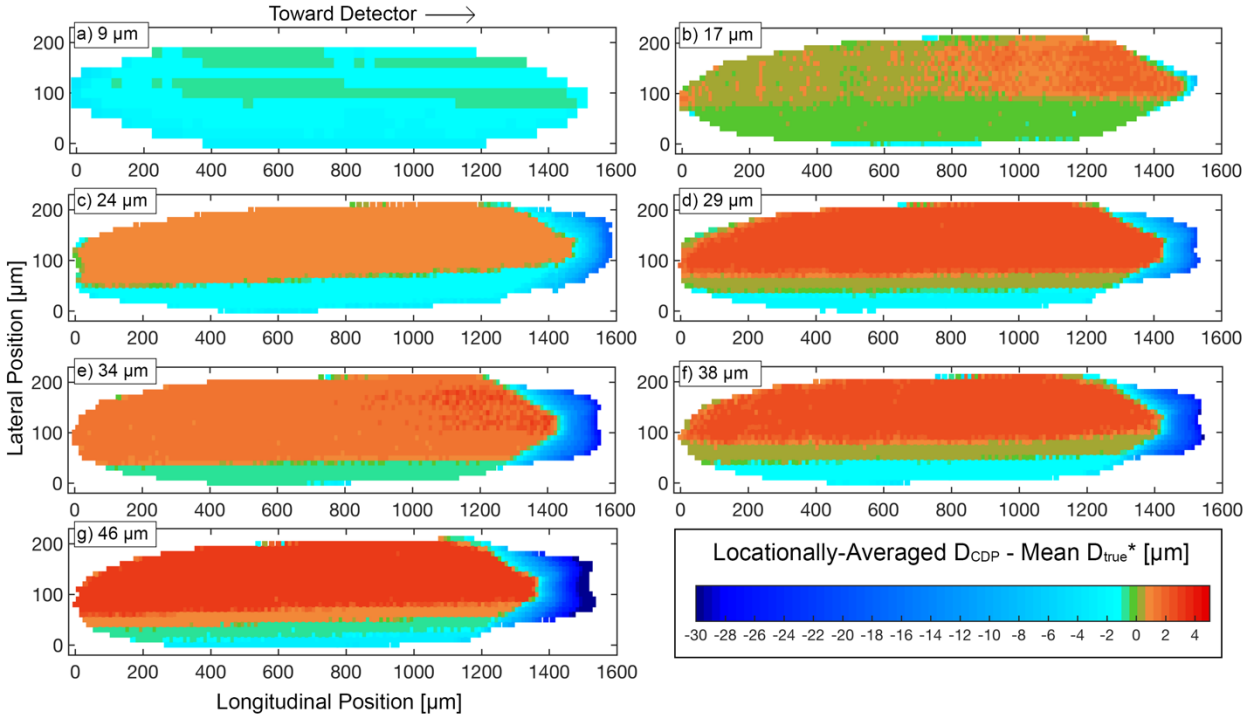

Figure 3.6 - *The difference of D_{CDP} averaged at each sample location and mean D_{true}* for each calibration. Warm colors indicate locations where the CDP oversized droplets, cool colors show areas that droplets were undersized. The maps' right side is closest to the detector.*

Figure 3.6 reveals that all but the 9 μm calibration show a similar lateral gradient in sizing accuracy. The lower 1/3rd to 1/4th of the sample area tend to truthfully or slightly undersize droplets (shown by shades of green and blue) and the upper 2/3rd to 3/4th of the sample area shows a fairly homogenous tendency to oversize droplets by approximately 2 – 4 μm. This lateral gradient of sizing accuracy appears in Figure 3.5 as the spreading and rightward skewing of D_{CDP} distributions relative to D_{true}* distributions. CDP calibrations performed by Lance et al. in 2010 revealed a similar lateral gradient in sizing accuracy. Lance et al. concluded that this behavior is likely due to "Misalignment of the qualifier mask relative to the axis of the laser beam" which affects the amount of light reaching the collecting optics by altering forward scattering angles (Lance et al., 2010). The researchers demonstrated that observed gradients in sizing accuracy could be caused by a 1 mm misalignment of the laser beam relative to the collecting optics. Although Lance et al.'s misalignment calculations cannot be directly applied to the findings presented here (misalignment severity is expected to be instrument-specific) it is possible that a similar issue affects the UWKA CDP.

Lance et al. (2010) concluded that "Droplets are systematically oversized by up to 20%" but the researchers based these finding on nine calibrations that only tested sizing accuracy at the center of the sample area. If sizing accuracy from our tests is only considered at the center of the sample area, it would appear that the UWKA CDP systematically oversizes droplets by as much as 15%. But using sizing responses from all sample locations indicates that the overall impact of oversizing is less severe

because droplets are also undersized in a significant number of sample locations. If sizing accuracy is considered for all sample locations, absolute sizing error is less than 3% for droplets larger than 9 μm.

Missizing of droplets will impact higher moments including mean diameter (D_{Mean}), effective diameter (D_{eff}), and volume-weighted mean diameter (VMD). Figure 3.7 shows the difference between D_{Mean}, D_{eff}, and VDM when calculated with distributions of D_{CDP} vs. distributions of D_{true}*. For the calibration runs presented here, missizing affects D_{Mean} (black crosses) by less than ±1.0 μm for all D_{true} greater than 9 μm. Differences of D_{Mean} for the calibration runs with diameters greater than 30 μm, is less than ±0.2 μm.

D_{eff} (blue crosses in Figure 3.7) and VMD (red crosses) are more greatly impacted by missizing than D_{Mean} (especially for larger droplets) which is not surprising considering that D_{eff} and VMD incorporate higher order moments of size distributions. The difference between D_{eff}, VMD, and D_{Mean} calculated with D_{CDP} vs. D_{true}* are similar for droplets smaller than 29 μm but begin to diverge for droplets that are 34 μm or larger. Difference in D_{eff} and VMD is approximately 1.5 μm greater than D_{Mean} difference for 46 μm droplets. All-in-all, sizing error is expected to cause less than 2 μm uncertainty in D_{Mean}, D_{eff}, or VMD for droplets of 9 – 46 μm diameter.

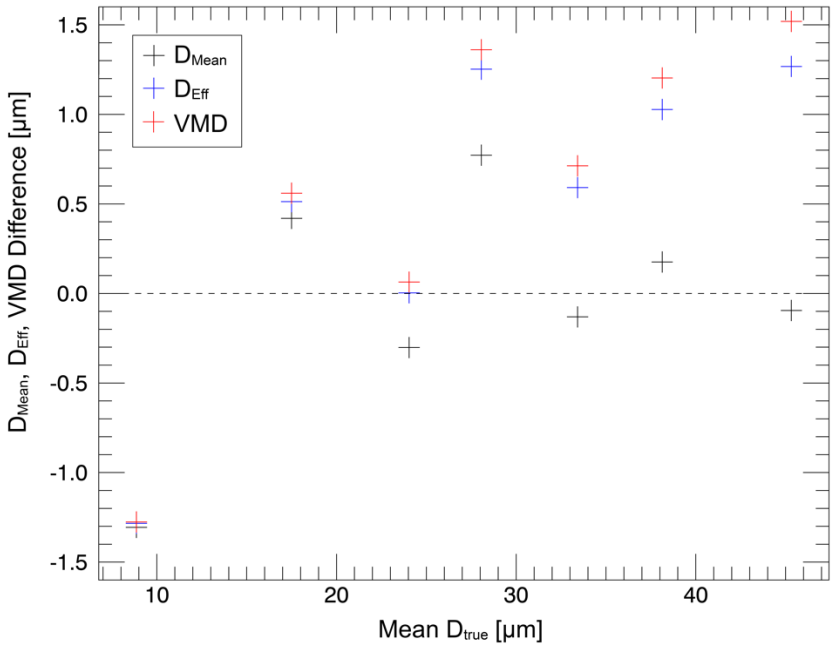

Figure 3.7 - *Difference (each statistic calculated with D_{CDP} minus each statistic calculated with D_{true}*) of D_{Mean} (black), D_{eff} (blue), and VMD (red) for all seven calibrations.*

3.4.2 - Droplet counting performance

The seven calibrations indicate that the CDP has similar locational-dependent counting performance when detecting 9 – 46 µm diameter droplets. Figure 3.8 shows beam maps of counting accuracy and reveals that errors in counting are less than ±10% for a majority of sample area locations (green areas). In fact, count error is less than ±1% for approximately 85% of sample area locations.

Count error is more significant (varying from 20 to 100% undercounting) around the sample area perimeter (shown by blue and purple locations). Though it appears that counting performance is poor around the sample area boundaries The fact that droplets

are undercounted around the sample area perimeter has important implications regarding measurements of sample area dimension (discussed in the following section).

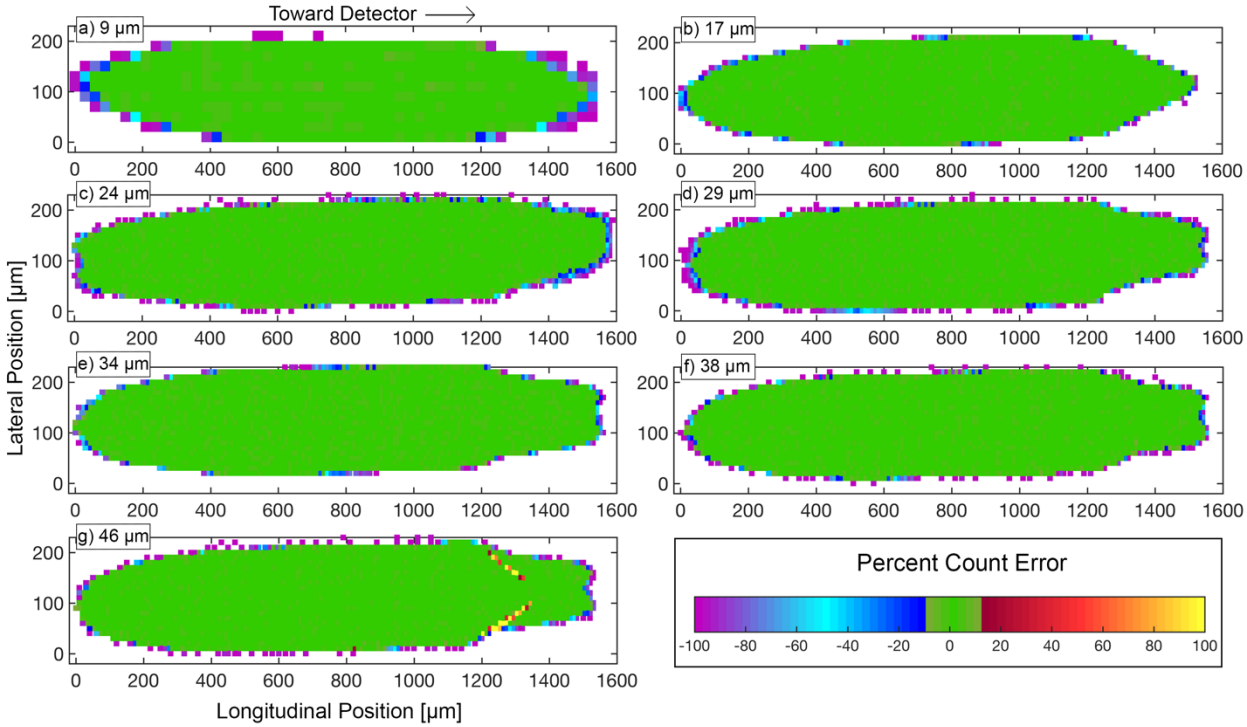

Figure 3.8 - *Beam maps of percent count error (percent difference of CDP counts vs. actual droplet counts calculated from printhead ejection frequency) for each calibration (indicated in upper-left corner). Green signifies absolute count error less than 10%, warm colors signify count error between 10 and 100%, and cool colors signify count error between -10 and -100%. The maps' right side is closest to the detector.*

Only the 46 µm calibration revealed regions where droplets are significantly overcounted. When detecting 46 µm droplets, the CDP overcounted by 30% – 100% (regions of red and yellow in Figure 3.8g) just left of the region where 46 µm drops are severely under sized (blue area on the right side of Figure 3.6g). This "overcounting region" covers approximately 0.9% of the sample area. For overcounting to occur, detector responses must vary so that the normalized qualifier signal exceeds, drops

below, and then again exceeds sizer signal during the transit of a droplet. It seems likely that variations in qualifier response are primarily responsible for overcounting because droplets passing through the overcounting region are subject to less than 5% missizing (this *hints* that sizer response is relatively unaffected).

To evaluate each calibration's counting performance, percent count error is calculated as the percent difference between the sum of CDP-recorded counts and the sum of expected counts calculated from the printhead droplet ejection frequency. Percent count error is calculated three ways for each calibration by filtering which sample locations are included in the calculation by what percentage of actual counts they received. For example, percent count error calculated using a 50% count threshold would only consider count error at sample locations where the ratio of recorded droplet counts to actual droplet counts is at least 0.5. Percent count error is calculated using count thresholds of 10%, 50%, and 90% of expected counts. This "count threshold" method both provides a range of count error and considers the fact that a fraction of droplets were placed beyond a 10 μm x 10 μm region (refer to Figure 3.4 in Section 3.3.2).

CDP counting accuracy is relatively similar for droplets of 17 – 46 μm diameter. Figure 3.9 shows that absolute percent count error (calculated using count thresholds of 10%, 50%, and 90% actual counts) is between 1.0% and 2.3% for all but the 9 μm calibration. Percent count error is greater than 0% for only the 46 μm calibration (due to the two regions of overcounting shown in Figure 3.8g). 9 μm droplets are most undercounted; has a percent count error range of approximately -1% to -5%. It is possible that the

lower bound of 9 μm percent count error is exaggerated due to that calibration's lower spatial resolution.

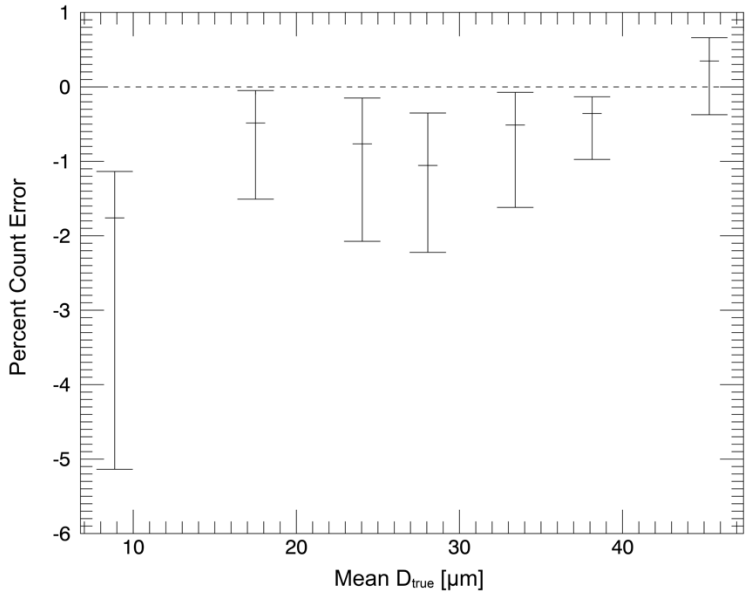

Figure 3.9 – *Percent count error for each calibration. Top and bottom bars show percent count error calculated using 10 and 90% count thresholds. Central horizontal line is calculated using a 50% count threshold.*

Count error introduces uncertainty in concentration and LWC measurements that are proportional to percent count error. Therefore, it is expected that counting error introduces less than 2.2% absolute error in concentration and LWC for 17 – 46 μm droplets. Counting error for 9 μm droplets is estimated to introduce as great as 5.2% absolute error in concentration and LWC.

Lance et al.'s 2010 work also found that droplets were counted to within 4% accuracy for interior sample locations. Locations around the perimeter of the sample area were subject to significant undercounting and overcounting. The researches stated that

overcounting at boundary locations is a result of electronic noise when sizer and detector signals are of similar magnitudes. It is not immediately clear why our tests did not show similar patterns of overcounting.

Instrument response limitations could cause counting error to vary with airspeed. The time that a detector diode is illuminated by scattered light is inversely related to airspeed. It is conceivable that slow instrument response could decrease detector signals and lead to more significant undercounting as airspeed increases. This work tested CDP performance at a simulated airspeed of ~32 m s^{-1} (~1/3rd typical UWKA airspeed) so additional calibrations using greater droplet velocity would need to be performed to test how counting (and/or sizing) accuracy is affected by airspeed.

3.4.3 - Measurements of sample area dimension

Higher DSD moment calculations require knowledge of the sample volume, which is the product of the sample area (SA) and true airspeed. Error in SA leads to bias in higher moments including concentration and LWC. SA calculations use the same "count threshold" method described in paragraph four of Section 3.4.2. SA is calculated as the product of the number of sample locations that meet the respective count threshold criteria and the area of a single sample location (600 μm^2 for the 9 μm calibration or 100 μm^2 for all other calibrations).

Figure 3.10 shows SA calculated with 10, 50, and 90% count thresholds ($SA_{10\%}$, $SA_{50\%}$, $SA_{90\%}$) as black bars and illustrates that SA varies with changes in D_{true}. SA is smallest

for 9 and 17 µm droplets ($SA_{50\%}$ is ~0.255 mm^2), reaches a maximum $SA_{50\%}$ of 0.281 mm^2 at D_{true} of 24 µm, and decreases to 0.268 mm^2 by D_{true} of 46 µm. Overall, SA varies by 0.03 mm^2 (~10% variance).

The range of SA for D_{true} of 9 – 17 µm is similar to the SA range for D_{true} of 24 – 29 µm ($SA_{50\%}$ range = 0.009 and 0.011 mm^2 respectively). 38 and 46 µm droplets have the smallest $SA_{50\%}$ range (0.004 mm^2) and smallest $SA_{10\%}$ - $SA_{90\%}$ range; presumably because larger droplets scatter more light at greater scattering angles and are more consistently detected at sample area boundaries.

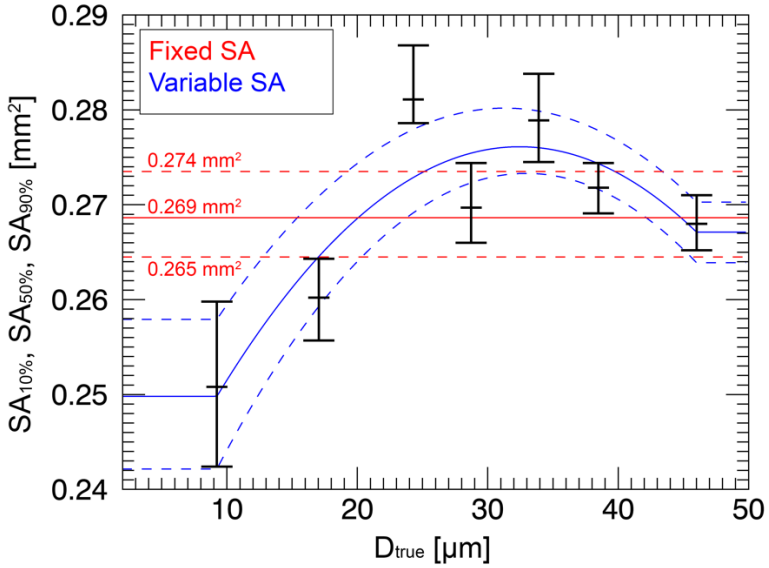

Figure 3.10 – *Black bars show SA measured for each calibration calculated using actual count thresholds of 10, 50, and 90% ($SA_{10\%}$, $SA_{50\%}$, $SA_{90\%}$). Red shows fixed (mean) $SA_{10\%}$, $SA_{50\%}$, and $SA_{90\%}$ (with fixed SA values shown on the left) and blue shows a second-degree polynomial fit to $SA_{10\%}$, $SA_{50\%}$, and $SA_{90\%}$. Variable SA is held constant for D_{true} less than 9 µm or greater than 46 µm.*

SA values used for concentration calculations can be provided in one of two manners: using a 'fixed' SA equal to the mean of $SA_{50\%}$ for all droplet sizes (solid red line in Figure 3.10) or using a 'variable' SA estimated with a second-degree polynomial fit to $SA_{50\%}$ (solid blue line). Note that variable SA is set to a constant value for D_{true} beyond 9 and 46 μm.

To investigate the impact of using a fixed vs. variable SA, three Poissonian DSDs (with means of 10, 25, and 35 μm) are prescribed and LWC/concentration are calculated using both fixed and variable SA. The concentration of each DSD equals 100 cm^{-3} when calculated with fixed SA (0.269 mm^2). To provide estimates of how SA uncertainty impacts derived values, LWC and concentration are also calculated using $SA_{10\%}$ and $SA_{90\%}$ (dashed blue and red lines).

Table 3.3 shows results for variable SA vs. fixed SA calculations and lists variable $SA_{50\%}$ concentration, variable $SA_{50\%}$ LWC, fixed $SA_{50\%}$ LWC and the percent difference of variable $SA_{50\%}$ LWC vs. fixed $SA_{50\%}$ LWC. Fixed $SA_{50\%}$ concentration is not shown because it equals 100 ± 1.67 cm^{-3} for all DSDs (uncertainty range = [fixed $SA_{10\%}$ concentration – fixed $SA_{90\%}$ concentration] / 2). Using fixed vs. variable SA affects concentration and LWC for the 10 μm distribution the most (variable $SA_{50\%}$ concentration is 6.0% greater and variable $SA_{50\%}$ LWC is 4.2% greater). Using fixed vs. variable SA changes concentration and LWC less than 2% for the 25 and 35 μm distributions.

Table 3.3 – Concentration and LWC calculated using variable $SA_{50\%}$, LWC calculated using fixed $SA_{50\%}$, and percent difference of LWC calculated using variable vs. fixed $SA_{50\%}$. Uncertainty range is one half the difference of each parameter calculated using $SA_{10\%}$ and $SA_{90\%}$.

Distribution Mean [μm]	Variable $SA_{50\%}$ Conc. [cm^{-3}]	Variable $SA_{50\%}$ LWC [g m^{-3}]	Fixed $SA_{50\%}$ LWC [g m^{-3}]	% Diff Variable $SA_{50\%}$ LWC vs. Fixed $SA_{50\%}$ LWC
10	105.990 ± 3.063	0.0820 ± 0.0021	0.0787 ± 0.0013	4.21
25	98.785 ± 1.586	0.9252 ± 0.0134	0.9426 ± 0.0157	-1.84
35	97.923 ± 1.195	2.2941 ± 0.0272	2.3378 ± 0.0390	-1.87

Using a fixed value of SA = 0.27 mm^2 for concentration and LWC calculations is most appropriate given that using fixed vs. variable estimates of SA result in less than 6% difference in concentration and less than 5% difference in LWC. The 10 μm distribution has the largest percent difference in LWC (variable $SA_{50\%}$ LWC is 4.21% greater) but the actual difference in LWC is insignificant (0.0033 g m^{-3} greater for variable $SA_{50\%}$) because small droplets contribute relatively little mass. It furthermore is excessive to parameterize SA's droplet size dependence because it is not known how SA behaves for D_{true} between the tested sizes.

3.4.4 - LWC error due to sizing and counting error

Error in calculated LWC can be contributed by sizing error and counting error. Counting error introduces percent LWC error proportional to percent count error. Error in droplet size will cause percent LWC error proportional to third power of error in droplet diameter (or using notation introduced at the beginning of Section 3.4, percent LWC error ≈ $D_{CDP}{}^3 - D_{true}{}^{*3}$).

Figure 3.11 shows estimates of percent LWC error that would be introduced by sizing error (red) and the combined effects of sizing and count error (black). It shows that LWC error is most affected by missizing. 9 μm droplets are subject to both the most absolute and the greatest range of percent LWC error. Percent LWC error for 9 μm droplets has a greater range than other droplet sizes because percent count error is more variable; presumably due to the coarse spatial resolution used during the 9 μm calibration. 9 μm droplets contribute relatively little water mass so it is less likely that percent LWC error for 9 μm droplets will significantly impact LWC measurements in most circumstances.

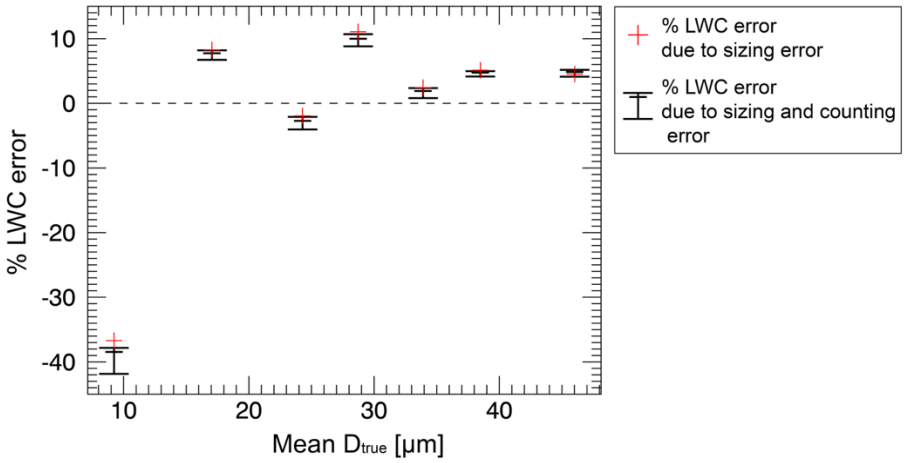

Figure 3.11 – *Estimates of percent LWC error due to sizing error (red), and percent LWC error due to both sizing and count error (calculated using 10, 50, and 90% count thresholds). Percent LWC error due to sizing error is calculated as the percent difference between the integrated normalized distribution of* $(D_{CDP})^3$ *and the integrated normalized distribution of* $(D_{true}*)^3$ *(the distributions shown in Figure 3.5).*

Percent LWC error for D_{true} of 17 and 29 μm (~8 and 10% respectively) is greater than that for other droplet sizes. Total percent LWC error, excluding estimates for 17 and 29 μm droplets, could be modeled reasonably well using a second-degree polynomial fit

that would begin with significantly negative percent error for D_{true} of 9 μm and asymptote to ~5% by D_{true} of 38 μm. Percent LWC error for D_{true} other than 17 and 29 μm indicates that LWC could be underestimated by as much as 42% for 9 μm droplets, underestimated by ~3% for 24 μm droplets, overestimated by ~2% for 34 μm droplets, and overestimated by ~5% for 39 and 46 μm droplets.

3.5 – Concluding remarks

The calibration of the UWKA CDP was evaluated using water droplets with diameters of approximately 9, 17, 24, 29, 34, 38, and 46 μm. The evaluations tested sizing and counting accuracy at discrete locations that covered the entire sample area (the 17 – 46 μm calibrations tested CDP response at ~4600 locations and the 9 μm calibration tested ~460 locations). Calibrations also provided measurements of sample area dimensions.

The CDP shows a similar lateral gradient in sizing accuracy for the 17 – 46 μm calibrations where locations in the upper 2/3^{rds} of the sample area tended to oversize droplets by 2 – 4 μm and the lower 1/3rd either accurately sized or undersized droplets by ~2 μm. The severity of oversizing is correlated to the diameter of measured droplets. The 17 – 46 μm calibrations also revealed that the rightmost 6 – 9% of the sample area under sizes droplets by ~20 μm. The locational variability of sizing accuracy causes an artificial spreading of DSDs that could be mistakenly attributed to natural DSD broadening processes. The 9 μm calibration does not show a lateral gradient in sizing accuracy similar to what is observed for 17 – 46 μm droplets. Instead, 9 μm droplets are undersized by approximately 2 μm across ~90% of the sample area. This systematic

sizing bias does not appreciably widen DSDs when measuring 9 μm droplets but does cause a 1.3 μm underestimation of mean droplet diameter.

For all droplet sizes, counting error is less than ±1% for ~85% of the total sample area but regions along the sample area boundary do tend to undercount droplets by ~20 - 90%. Overall counting accuracy is not greatly affected by undercounting at sample area boundaries because these regions account for less than 5% of the total sample area. For droplets of 17 – 46 μm diameter, overall count error is less than 2%. Mis counting is more severe for 9 μm droplets but results in less than 5% undercounting. Counting error affects higher moment calculations and introduces error in concentration and LWC proportional to percent count error. It is expected that counting error can cause less than 5% underestimation of concentration/LWC for 9 μm droplets and less than 2% absolute error in concentration/LWC for all other droplet sizes.

Measurements of sample area reveal that $\mathrm{SA}_{50\%}$ averaged for all calibrations equals 0.269 mm^2. SA is somewhat dependent on $\mathrm{D}_{\mathrm{true}}$ ($\mathrm{SA}_{50\%}$ varies by ~0.03 mm^2 or ~10%). It is suggested that SA measurements for higher moment calculations can be provided by either using a fixed mean SA or a variable parameterization of SA using a second-order polynomial fit of SA vs. $\mathrm{D}_{\mathrm{true}}$. Concentration and LWC are calculated for three Poissonian distributions with mean diameters of 10, 25, and 35 μm using fixed and variable SA. Using the two SA parameterizations results in less than 6% difference in concentration and less than 5% difference in LWC. Therefor it is most logical to simply use a fixed SA = 0.27 mm^2 for higher moment calculations.

Error in sizing and counting can contribute to error in computed LWC. It is expected that the mentioned factors can cause LWC to be underestimated by 38 – 42% for 9 μm droplets. For droplet diameters between 17 – 29 μm percent LWC error could realistically range from -4 – 11%. LWC for droplets larger than 29 μm is likely to be overestimated by no greater than 6%. Small droplets contribute relatively little mass so it is less problematic that percent LWC error is greatest for 9 μm droplets.

Chapter 4 will discuss additional sources of uncertainty including CDP coincidence error and Nevzorov collection efficiency effects. Examples of Nevzorov measurements taken in various cloud phases are presented and the effects of several uncertainty sources are discussed. Chapter 4 also uses intercomparisons of LWC from CDP and Nevzorov measurements to provide an in-situ analysis of uncertainty caused by many factors including Nevzorov convective heat losses (Chapter 2), collection efficiency effects, and CDP missizing, miscounting, and coincidence error (Chapter 3).

4 – Analysis of in-situ Nevzorov and CDP measurements

This chapter introduces several sources of uncertainty in CDP and Nevzorov measurements beyond those discussed in chapters 2 and 3. Examples of Nevzorov measurements taken in liquid cloud, mixed phase cloud, ice cloud, and a region of supercooled drizzle are presented. Finally, PACMICE and SNOWIE data are used to compare LWC measurements from the Nevzorov and CDP to further investigate how uncertainty can affect both instruments. Findings from LWC comparisons are compared to results from chapters 2 and 3.

4.1 – Sources of uncertainty in Nevzorov measurements

Chapter 2 demonstrated that Nevzorov calculations require the removal of convective heat losses which would otherwise cause an overestimation of TWC and LWC. Calculations include a convective heat loss coefficient (k) that changes with variations in flight level and airspeed. k drift due to variations in flight level and airspeed introduces TWC and LWC uncertainty that manifests as baseline drift. A k calibration method was developed that minimizes the effects of k drift. ~35,000 clear air points were used to estimate MDS TWC/LWC (95th percentile residual TWC/LWC) and TWC/LWC uncertainty caused by k drift (5th – 95th percentile range of TWC/LWC) in conditions devoid of instrument icing. MDS TWC is 0.01 g m^{-3} and k drift is expected to cause 0.02 g m^{-3} uncertainty in TWC. MDS LWC is estimated to be 0.02 g m^{-3} with k drift contributing to 0.03 g m^{-3} LWC uncertainty.

There are several factors in addition to k drift that can cause uncertainty in TWC and LWC. Collector sensors cause flow distortion which can alter particle trajectory and decrease the number of particle/collector sensor interactions. This effect is referred to as collection efficiency and leads to an underestimation of TWC and LWC (Korolev et al., 1998). Sensor saturation occurs when insufficient power is available to evaporate all impinging particles and also causes an underestimation of TWC and LWC (Emery et al., 2004). Effects specific to ice particle interacts can also introduce uncertainty in TWC and LWC measurements. Ice particles can rebound off the surface of the TWC collector which leads to TWC underestimation (Emery et al., 2004). The LWC sensor is designed to minimally interact with ice particles but residual interactions can cause LWC overestimation (Korolev et al., 1998).

4.1.1 – Additional sources of Nevzorov TWC uncertainty

TWC droplet collection efficiency has been parameterized in model-based (Korolev et al., 1998), wind tunnel (Strapp et al., 2003), and in-situ (Schwarzenboeck et al., 2009) studies. Less is known about TWC ice collection efficiency (TWC_{ICE}) due to lack of reliable independent measurements of ice water content (IWC) and the fact that it is difficult to create precisely-sized ice particles in wind tunnel studies.

Figure 4.1 shows parameterizations of TWC and LWC droplet collection efficiency. TWC droplet collection efficiency estimates for droplet VMD of 0 – 25 μm are provided by Korolev et al. (1998) and estimates for VMD of 25 – 300 μm are an extrapolation of Korolev et al.'s finding (Strapp et al., 2003 and Schwarzenboeck et al., 2009). TWC

collection efficiency for small droplets is much less than unity (.1 for VMD of 3 μm, increasing to .6 for VMD of 10 μm) because droplets with insignificant mass are unable to cross streamlines and tend to be swept around the TWC sensor. Larger droplets are more capable of crossing streamlines so TWC collection efficiency increases to .9 at 25 μm VMD and continues to approach unity for larger droplets.

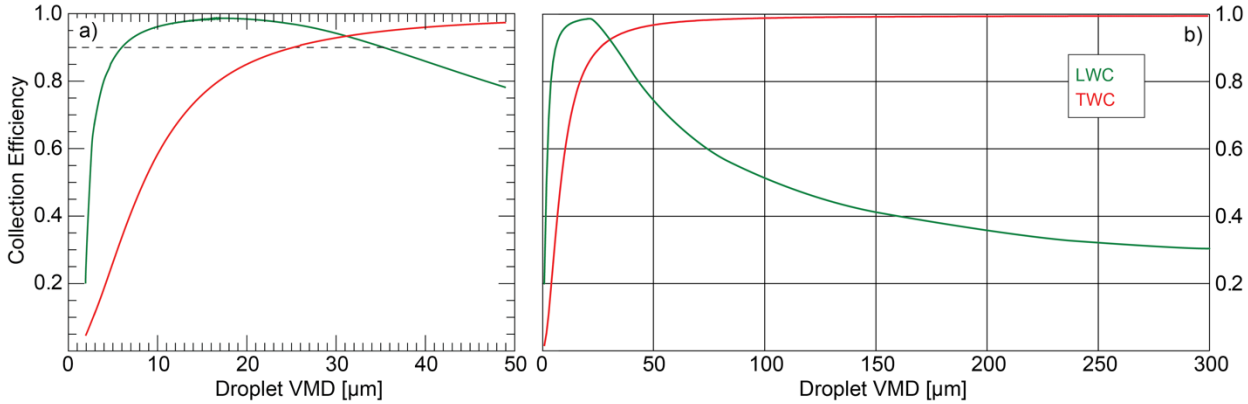

Figure 4.1 - *TWC (red) and LWC (green) droplet collection efficiency plotted as a function of droplet VMD. Collection efficiency parameterizations for 0 – 25 μm VMD are from Korolev et al. (1998). TWC collection efficiency from 25 – 300 μm VMD is an extrapolation of Korolev et al.'s parameterization. LWC droplet collection efficiency for 25 – 300 μm VMD is from in-situ studies by Schwarzenboeck et al. (2009).*

Particle size dependent parameterizations of TWC ice collection efficiency have yet to be developed but it is known that ice particles can splinter on contact with the TWC collector, rebound, and get swept away before they are completely evaporated. This "ice rebounding" effect causes TWC to be underestimated. To minimize ice rebounding, a modified "deep cone" TWC sensor was developed with an apex angle that is 60° (compared to the "standard" sensor's 120°). A 2013 study by Korolev et al. used high speed cameras to investigate the effectiveness of the deep cone design. They found

that the deep cone sensor measured 3 times more IWC than the standard sensor (Korolev et al., 2013). The UWKA Nevzorov features the deep cone design so it is assumed that IWC error caused by ice rebounding is less of a concern.

Korolev et al.'s 2013 study also showed that the TWC sensor is affected by pooling (also called sensor saturation) which occurs when insufficient power is available to evaporate all collected water so it accumulates in the base of the TWC collector cone. Pooling causes TWC to be underestimated and can skew the TWC signal's temporal relationship. Pooling affects the standard TWC sensor for measurements greater than 0.7 g m^{-3} (Korolev et al., 2013). The researchers were not able to assess how pooling impacts deep cone TWC sensors. Pooling is likely to introduce negligible error for the data presented in this chapter because TWC measurements during PACMICE and SNOWIE rarely exceeds 0.7 g m^{-3}. The UWKA Nevzorov also features circuitry designed to minimize the occurrence of pooling by providing greater amounts of current.

4.1.2 Additional sources of Nevzorov LWC uncertainty

As with TWC measurements, non-unity droplet collection efficiency can cause underestimation of LWC. For small droplets, LWC droplet collection efficiency is significantly greater than TWC collection efficiency because the rod-shaped LWC sensor causes less streamline distortion than the inverted cone design of the TWC sensor. Figure 4.1a shows that Korolev et al.'s (1998) model suggests that LWC collection efficiency is much less than unity for droplet VMD of 3 μm, rapidly increases to .9 by 8 μm VMD, and is very near unity by VMD of 17 μm. LWC collection efficiency begins to

depart from unity for droplets larger than 17 μm because larger droplets are prone to being swept off of the LWC sensor before they are completely evaporated. Incomplete droplet evaporation causes LWC collection efficiency to be approximately 0.4 at 150 μm VMD and ~0.3 by 300 μm VMD.

The LWC collector sensor is designed to cause impinging ice particles to shatter and be swept away before they can melt and evaporate. In reality, ice particles do cause some degree of LWC sensor cooling. A particle size dependent parameterization of how the LWC collector responds to ice particles is not available but Korolev et al. (1998) estimated that in ice cloud, LWC will erroneously be measured as 11% of IWC.

4.2 – CDP coincidence error

Chapter 3 focuses on work with a droplet generating calibration system designed to investigate CDP error caused by gradients in laser intensity, component misalignment, and error in measurements of SA. Coincidence error is another source of uncertainty that can not be directly explored using the calibration system.

Coincidence is a concentration-dependent phenomenon that occurs when two or more droplets are simultaneously within a CDP's sample area. The effect can cause error in both droplet counting and droplet sizing (Lance et al., 2010). Missizing can occur if coincident droplets scatter additional light into the collecting optics. Missizing severity depends on many factors including the size, number, and position of coincident droplets. Coincidence will always cause undercounting because the CDP is capable of

only counting/sizing a single droplet at a time. Miscounting is more severe if coincident light causes sizer voltage to exceed threshold values, which causes all droplets within the sample area to be rejected. Because CDP sample area is relatively small (SA for the UWKA CDP's measured as 0.27 mm^2), coincidence is expected to only impact CDP measurements in high droplet concentrations.

Lance et al. (2010) describe a region surrounding the sample area as the "extended sample area" where transiting droplets are not sized/counted but are capable of scattering light into the collecting optics. Lance et al. investigated the potential impacts of "extended coincidence error" which occurs when droplets are simultaneously within both the "standard" sample area and extended sample area. The researchers found that extended coincidence is much more likely to occur than standard coincidence because the extended sample area (20.1 mm^2) can be much larger than the standard sample area (~0.3 mm^2) (Lance et al., 2010). Extended coincidence can cause qualified droplets (those passing through the standard sample area) to be oversized. It can also cause undercounting if coincidently-scattered light causes sizer responses to exceed threshold values (Lance et al., 2010). The researches concluded that extended coincidence can cause as much as 60% oversizing and 50% undercounting at droplet concentrations of 400 cm^{-3}. Lance et al. also found that the combined effects of gradients in laser intensity, component misalignment, SA error, standard coincidence, and extended coincidence can lead to a 40% overestimation of LWC at measured concentrations of 200 droplets cm^{-3} or a 110% LWC overestimation in measured concentrations of 400 droplets cm^{-3} (see Figure 4.2). *Note: for the remainder of this*

chapter error in LWC and concentration due to the combination of laser intensity gradients, component misalignment, standard coincidence, and extended coincidence will be called error due to "all factors".

Lance et al.'s 2010 work motivated the development of a sizing detector pinhole mask designed to decrease the dimensions of the extended sample area (SA_E) and in turn mitigate the impact of extended coincidence. Follow up work (Lance et al., 2012) demonstrated that the pinhole mask reduced SA_E by an order of magnitude (20.1 mm^2 to 2.7 mm^2) and likewise decreased the occurrence of extended coincidence. The researchers estimated that CDPs with the pinhole mask modification were subject to less significant LWC error: 10% LWC overestimation at measured concentrations of 400 droplets cm^{-3} or 25% LWC overestimation at measured concentrations of 600 droplets cm^{-3}. Figure 4.2 (from Lance et al., 2012) shows the concentration dependent percent difference of CDP LWC vs. LWC measured by the Scientific Engineering Application (SEA) hotwire probe for both an unmodified and modified CDP. It shows that the percent difference of modified CDP LWC vs. SEA LWC is smaller and has less dependence on CDP concentration (7% difference / 100 cm^{-3} vs. 25% difference / 100 cm^{-3}). Work by Sulskis (2016) shows that coincidence error is negligible for droplet concentrations less than 1000 cm^{-3}. The UWKA CDP features this pinhole mask modification so it is expected that the impact of extended coincidence error is greatly reduced.

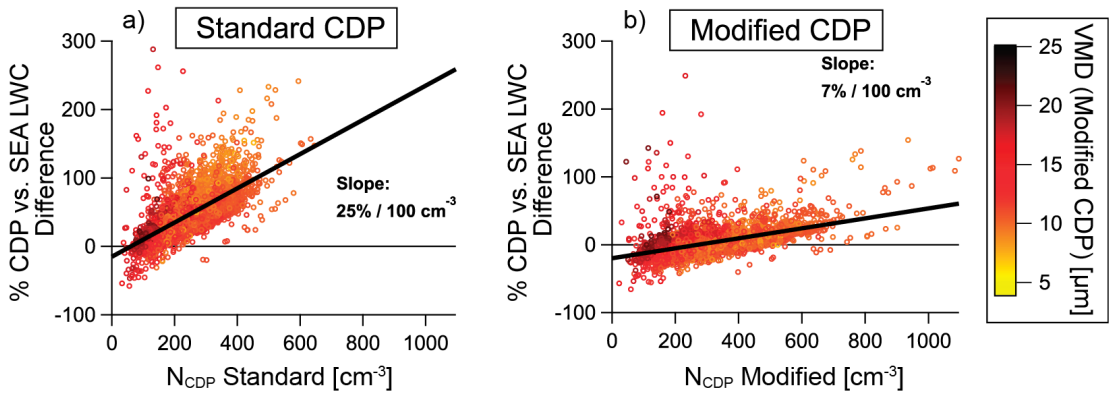

Figure 4.2 - *Percent difference of CDP LWC and LWC measured by the SEA hotwire probe plotted against CDP concentration (N_{CDP}). a) LWC difference for CDP without pinhole sizer mask. b) LWC difference for CDP with pinhole mask modification. Points are colored by modified CDP VMD. Taken from Lance et al., 2012.*

4.3 – Examples of Nevzorov measurements

Section 4.3 uses PACMICE and SNOWIE data to present four examples of Nevzorov measurements taken in liquid cloud, mixed phase cloud, ice cloud, and supercooled drizzle. An analysis of LWC, TWC, and IWC measurements and comments regarding uncertainty sources are provided.

4.3.1 – Liquid phase period

The following example uses data collected 20:34 – 20:38 UTC during an 08/26/17 PACMICE flight. It explores Nevzorov measurements in convective, non-precipitating, supercooled liquid cloud (5^{th} – 95^{th} percentile range of T = -19.8 to -14.0 C). The CDP indicated that cloud droplets had a 5^{th} – 95^{th} percentile VMD range of 9.9 – 18.1 μm and a 5^{th} – 95^{th} percentile concentration range of 72.6 – 666.6 cm^{-3}.

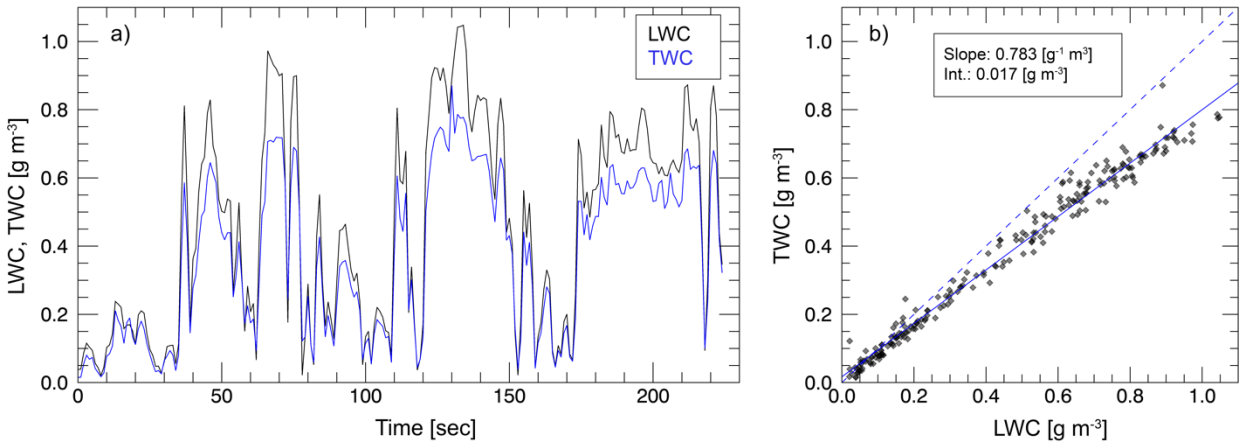

Figure 4.3 – *LWC vs. TWC plots for liquid phase period. a) LWC and TWC plotted verses time. LWC is shown as black line and TWC as blue. b) 1:1 scatter of TWC plotted against LWC. Dashed blue line is 1:1 line and solid blue line is a linear fit (slope and intercept are shown in legend).*

Figure 4.3a shows that the temporal response of the LWC and TWC signals closely resemble one another. Overall, LWC is greater than TWC (mean LWC = 0.43 g m^{-3}, mean TWC = 0.35 g m^{-3}). Figure 4.3b shows that TWC departs from LWC in a manner that is relatively consistent for all values of water content (by the fact that most points fall on the linear fit line). The linear fit slope in Figure 4.3b indicates that TWC is approximately 21.7% less than LWC. The difference between TWC and LWC can be attributed to droplet collection efficiency considerations which are expected to cause a ~23% mean percent difference between TWC and LWC for mean droplet VMD of 14.74 μm (Korolev et al., 1998).

4.3.2 – Ice phase period

A SNOWIE flight on 01/18/2017 collected data on the leading side of a deep, well-established system. Data for this ice-phase example are from a 22:39 – 22:50 UTC penetration flown at ~570 mb. The data have a 5th – 95th percentile T range -11.7 - -8.7 C. Ice particles were primarily 0.5 – 1.5 mm diameter dendrites, 1 – 1.5 mm aggregates, and 100 – 300 μm diameter oblate particles. Figure 4.4b shows 2DS buffer images captured during the period. CDP and Rosemount LWC had respective means of 0.002 and 0.001 g m^{-3} and support that no supercooled liquid droplets were present.

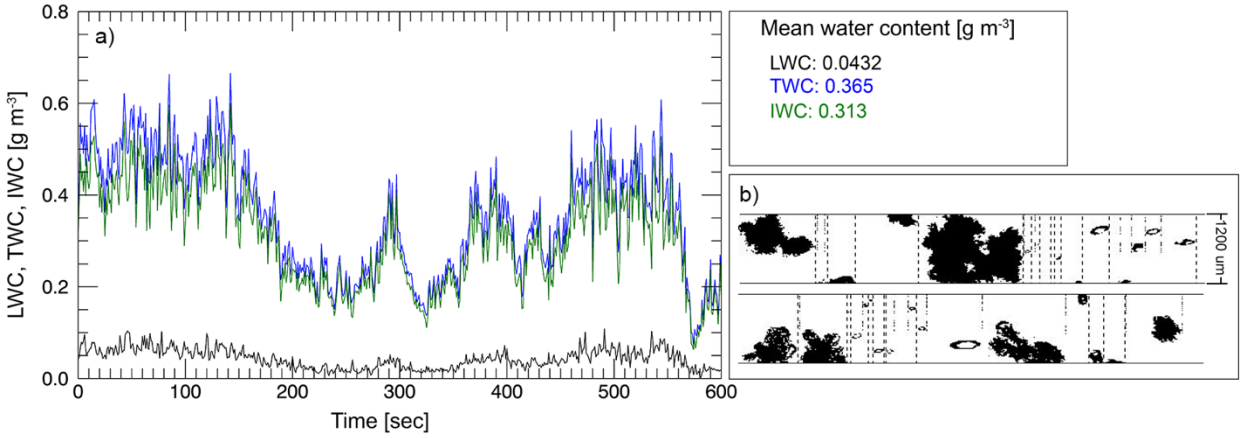

Figure 4.4 - *Ice phase plots. a) Time series showing LWC (black), TWC (blue), and IWC (green). Means and standard deviations are show in upper-right legend. b) 2DS buffer images of ice particles.*

Mean TWC equals 0.365 g m^{-3} and mean IWC is 0.313 g m^{-3}. TWC/IWC measurements are most likely minimally affected by ice rebounding because the UWKA Nevzorov uses a deep cone TWC sensor (Korolev et al., 2013).

Ideally in ice cloud, LWC would be less than MDS LWC (0.02 g m^{-3}) but Figure 4.4a shows that some water content was detected by the LWC sensor during the ice phase period (mean LWC = 0.043 g m^{-3}). It is likely that LWC measurements greater than MDS LWC are caused by interactions between the LWC collector and ice particles; a conjecture that is supported by the fact that LWC fluctuations roughly correlate with changes in TWC. Korolev et al. (1998) estimated that ice interactions will cause LWC to be ~11% of TWC. Mean LWC is 12.2% of mean TWC which is similar to Korolev et al.'s estimate.

Considering that error in LWC measurements introduces uncertainty in IWC, it may be more pertinent to simply consider IWC to be equal to TWC (instead of IWC = TWC – LWC) where other instruments can confirm the absence of liquid water.

4.3.3 – Mixed phase period

The UWKA encountered mixed phase conditions (5^{th} – 95^{th} percentile T range = -13.8 - -13.0 C) at 20:35 – 20:37 UTC during a 02/19/2017 SNOWIE flight. Particles were primarily 0.5 – 1 mm diameter aggregates, 100 – 150 μm long oblate ice, with a few columnar crystals, and cloud droplets with 5^{th} – 95^{th} percentile VMD range of 21.6 – 29.8 μm and 5^{th} – 95^{th} percentile concentration range of 13.0 – 72.5 cm^{-3}.

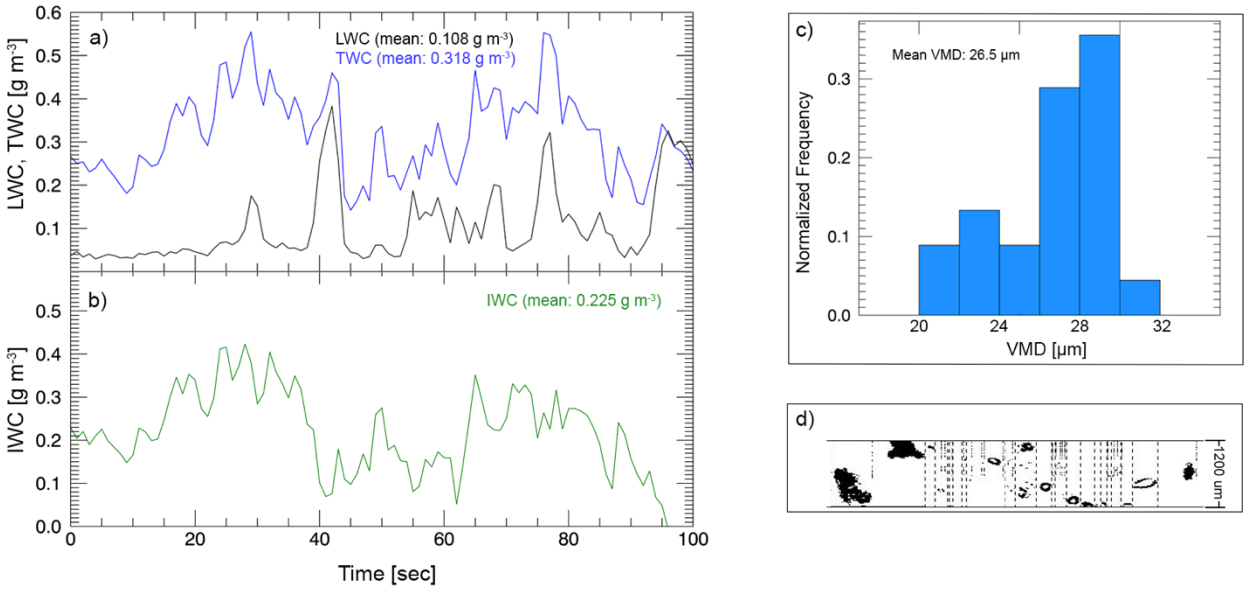

Figure 4.5 – *Plots for mixed phase period. a) Time series of LWC and TWC. b) Time series of IWC. c) VMD calculated from CDP DSDs. d) 2DS buffer images of particles encountered during period.*

Non-unity droplet collection efficiency is estimated to cause less than 8% underestimation of LWC and TWC and less than 2% underestimation of IWC. TWC sensor pooling is likely not an issue because TWC is less than 0.7 g m^{-3} (Korolev et al., 2013). Baseline LWC (typically 0.05 g m^{-3}) is greater than MDS LWC (0.02 g m^{-3}) which may be caused by ice impacts on the LWC sensor. It is not possible to provide exact estimates of LWC uncertainty caused by ice interactions without a suitable independent measurement of IWC. Likewise, it is not possible to quantitatively estimate how TWC ice collection efficiency and ice rebounding affect measurements during the period.

It is difficult to estimate Nevzorov uncertainty in mixed phase periods due to lack of independent IWC measurements, incomplete parameterizations of ice collection

efficiency, and unknowns regarding ice rebounding. For this example, LWC is relatively small compared to TWC. It would be more difficult to provide meaningful measurements of IWC in mixed phase conditions with greater LWC.

4.3.4 – Drizzle period

A SNOWIE mission on 03/09/2017 sampled cloud in a deep stratiform system that was producing widespread snow. While returning to base, the UWKA encountered a period (23:20 – 23:21 UTC) of supercooled (mean T = -3.82 C) 100 – 200 μm diameter drizzle at approximately 5,900 feet above ground level. Drizzle was intermixed with low concentrations of 1 mm diameter ice and cloud droplets (the CDP mean droplet concentration = 1.93 cm^{-3}). Figure 4.6b shows 2DS buffer images of drizzle and a typical ice particle.

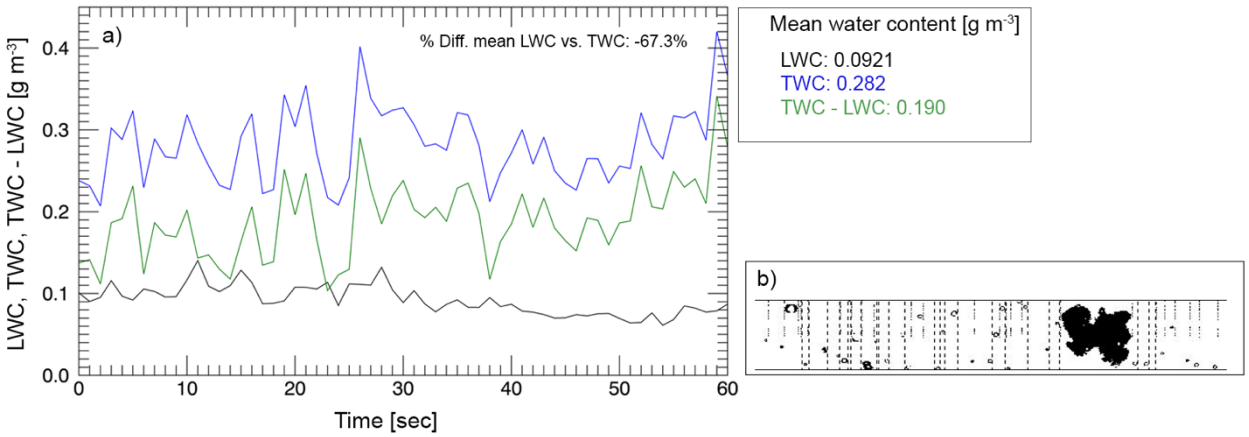

Figure 4.6 – *a) Time series showing LWC (black), TWC (blue), and TWC - LWC (green). Mean water contents are show in upper-right legend. b) 2DS buffer images of particles.*

It is likely that a majority of TWC – LWC difference (mean = 0.190 g m^{-3}) is due to droplet collection efficiency considerations. For 150 μm drops, TWC droplet collection efficiency

is very near 1 and LWC collection efficiency is near 0.4. This difference would cause an estimated -60% $\mathrm{TWC} - \mathrm{LWC}$ difference; a value similar to the actual percent difference of -67.3%. In an environment dominated by drizzle-sized drops, TWC serves as a better estimate of liquid water content but the presence of ice particles could compromise the validity of the substitution. Estimating the amount of uncertainty introduced by ice particles when using TWC to measure droplet water content would require additional (perhaps OAP) data.

4.4 – Comparison of Nevzorov and CDP LWC

This section uses comparisons of Nevzorov LWC ($\mathrm{LWC_{NEV}}$) and CDP LWC ($\mathrm{LWC_{CDP}}$) to further explore the previously discussed sources of uncertainty. It more specifically relates CDP calibration findings to results from in-situ LWC comparisons.

4.4.1 – Dataset overview

In-situ data provided by PACMICE and SNOWIE flights were manually analyzed to only include measurements taken in liquid only cloud (using IWC and 2DS buffer images). This phase analysis method minimizes uncertainty due to the presence of ice particles which causes $\mathrm{LWC_{NEV}}$ error (Korolev et al., 1998). Lance et al. (2010) suggested that the presence of ice may also result in overestimation of $\mathrm{LWC_{CDP}}$. To remove baseline noise and exclude periods when instruments were completely iced over, the selected data are further filtered to include only points where both $\mathrm{LWC_{NEV}}$ and $\mathrm{LWC_{CDP}}$ are greater than 0.05 g m^{-3}.

The filtering criteria produces a dataset of 18,047 1 Hz points that has a 5th – 95th percentile $\mathrm{LWC_{NEV}}$ range of 0.06 – 0.32 g m^{-3} and a 5th – 95th percentile $\mathrm{LWC_{CDP}}$ range of 0.07 – 0.46 g m^{-3}. Figure 4.7 shows dataset VMD and CDP concentration distributions separated by campaign. SNOWIE data comprise roughly 66% of the dataset. SNOWIE data have a 5th – 95th percentile VMD range of 17.5 – 36.6 μm and a 5th – 95th percentile concentration range of 10.9 – 67.5 cm^{-3}. PACMICE data have a 5th – 95th percentile VMD range of 14.8 – 26.5 μm and a 5th – 95th percentile concentration range of 94.2 – 535.5 cm^{-3}.

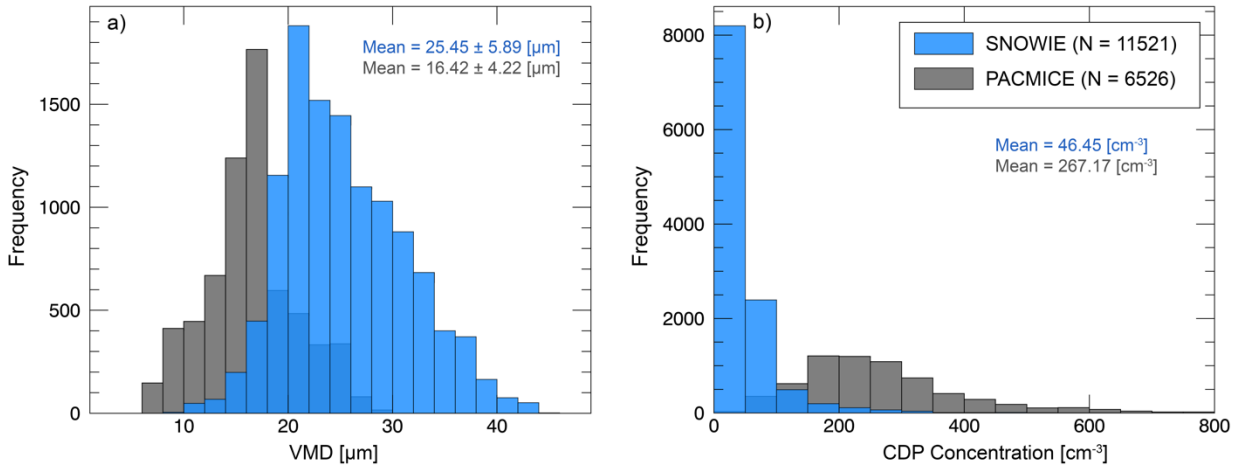

Figure 4.7 – *distributions of dataset a) VMD and b) CDP concentration. Blue and grey bars denote SNOWIE and PACMICE data respectively. Legend in b) includes number of points contributed from each campaign.*

The clouds encountered during SNOWIE did not have characteristics typical of continental clouds. Droplet concentrations were lower than expected (~70% of points had concentration less than 50 cm^{-3}) presumably due to scarcity of condensation nuclei. It is therefore unsurprising that droplet VMDs are also greater than those typically observed in continental clouds.

4.4.2 – LWC comparison results

Figure 4.8 shows VMD-binned mean percent difference of $\mathrm{LWC_{CDP}}$ vs. $\mathrm{LWC_{NEV}}$ calculated with a best fit line. Error bars show RMSE of $\mathrm{LWC_{CDP}}$. Green dashed lines are estimates of percent $\mathrm{LWC_{CDP}}$ vs. $\mathrm{LWC_{NEV}}$ difference that is caused by droplet collection efficiency effects and CDP missizing and miscounting (estimated using calibration results).

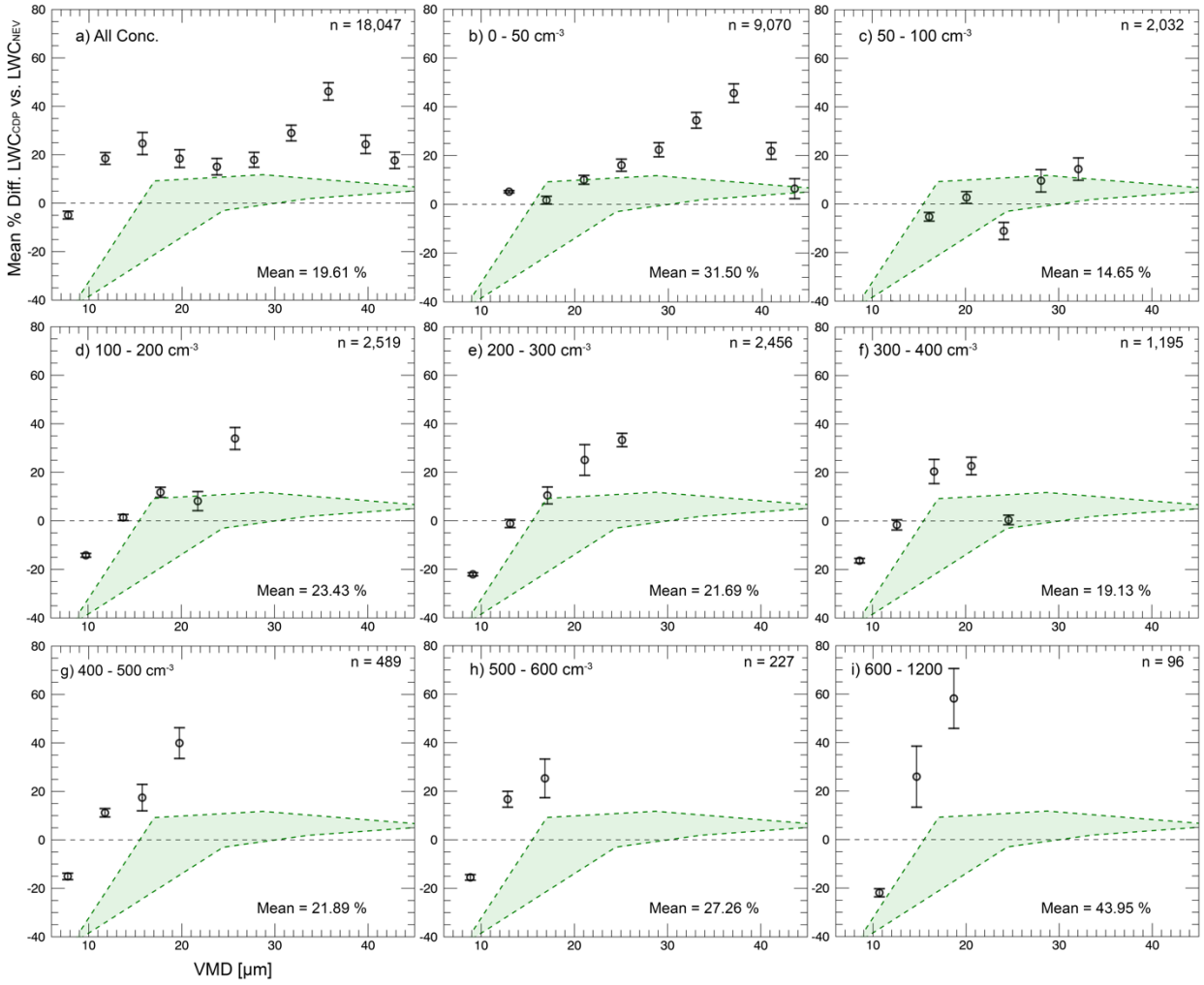

Figure 4.8 – *Mean percent difference of LWC_{CDP} vs. LWC_{NEV} calculated with a linear fit. A positive percent difference indicates that LWC_{CDP} is greater than LWC_{NEV}. Bars show RMSE of LWC_{CDP}. a) Percent difference for all data. b – i) Mean percent difference for data filtered by concentration. Mean percent difference for all data considered in each concentration range is*

listed in bottom right corner. Green dashed lines show estimates of percent difference that is caused by LWC droplet collection efficiency, and CDP missizing and miscounting.

It is expected, based on droplet generator results and Nevzorov droplet collection efficiency estimates, that the mean percent difference of $\mathrm{LWC_{NEV}}$ and $\mathrm{LWC_{CDP}}$ should be no greater than 15%. The actual mean percent LWC difference is 19.61%. Furthermore, Figure 4.8a shows that the percent difference between $\mathrm{LWC_{NEV}}$ and $\mathrm{LWC_{CDP}}$ is greater than the estimated difference for all VMD.

The discrepancy between estimated and actual percent LWC difference is not a result of coincidence error. Lance et al. (2012) concluded that coincidence is unlikely to affect measurements in concentrations less than 600 cm^{-3} and 2016 work by Sulskis indicated that coincidence is a non-factor in concentrations of less than 1000 cm^{-3}. Figures 4.8h and 4.8i show percent LWC differences for concentration ranges of 500 – 600 cm^{-3} and 600 – 1200 cm^{-3}, respectively. They show that mean percent LWC difference is comparatively greater in higher concentration ranges. Nonetheless, coincidence does not appreciably affect results when considering all data because only 1% of data have concentrations greater than 500 cm^{-3}.

Figure 4.8b shows that for concentrations of 0 – 50 cm^{-3}, the mean percent LWC difference is 31.5% with differences being as great as 45% for droplet VMD of 37 μm. Percent LWC difference is comparatively large for concentrations less than 51 cm^{-3} because data with low droplet concentrations have smaller LWC which can result in

baseline noise; especially when investigating percent differences. Data with concentrations of 0 – 50 cm^{-3} comprise 50% of the dataset but baseline noise cannot explain the discrepancy between estimated and actual percent LWC difference. Mean percent LWC difference is 23.40% if concentrations of 50 – 1200 cm^{-3} are considered.

CDP calibrations were conducted with a single droplet velocity that is ~30% of typical UWKA airspeeds so information about how counting, sizing, and SA vary with airspeed was not provided. It is possible that detector electronic response limitations could result in unpredictable changes in CDP performance or SA at higher airspeeds.

A direct correlation between SA and airspeed could explain the difference between estimated and observed percent LWC difference. The CDP records raw counts of particles that pass through the sample area as 'accepted particles' and those that pass through the extended sample area as 'depth-of-field rejected particles'. Given a large enough sample size, the ratio between accepted to depth-of-field rejected particles corresponds to the ratio of sample area to extended sample area. Therefore, a correlation between accepted vs. depth-of-field rejected particles and airspeed would suggest that SA is airspeed dependent. No such trends are evident to support that SA is airspeed dependent.

A direct relationship between the severity of oversizing and airspeed could also explain the discrepancy between estimated and actual percent LWC difference. Small errors in droplet diameter can greatly impact LWC estimates because LWC error is proportional to the third power of error in droplet diameter. It seems unlikely that electronic response

limitations would result in more significant sizing error but the notion warrants additional CDP calibrations using higher droplet velocity. Maximum droplet velocity is limited by the fact that droplet placement becomes less precise as velocity increases. Tests with greater droplet velocity could be conducted without system modification if spatial resolution is decreased.

Droplets would need to be overcounted on the order of 5% to account for the discrepancy between the estimated and actual percent difference of $\mathrm{LWC_{CDP}}$ vs. $\mathrm{LWC_{NEV}}$. Lance et al.'s 2010 droplet calibrations found that the CDP overcounts droplets by 4%. In contrast, the King Air CDP did not show significant overcounting. Only 46 μm droplets were overcounted by ~1%. Counting performance may simply be instrument specific. Nonetheless, it is worth repeating droplet calibrations with higher velocities to investigate if an airspeed dependence in counting performance can explain the discrepancy between estimated and actual percent LWC difference.

It is also possible that uncharacterized Nevzorov uncertainty sources are contributing to the discrepancy between estimated and actual percent LWC difference. Instrument icing was common during SNOWIE flights. It is possible that ice buildup on the vane of the Nevzorov alters collection efficiency which results in uncertainty in Nevzorov measurements. No studies have investigated the affects of vane icing so little more can be said about the hypothesis.

4.5 – Conclusions

There are several factors that can cause uncertainty in Nevzorov measurements. Drift in k causes uncertainty in TWC and LWC. When using the k calibration method presented in Chapter 2, k drift is expected to cause 0.02 g m^{-3} TWC uncertainty and 0.03 g m^{-3} LWC uncertainty in conditions devoid of instrument icing. It should be noted that vane icing may result in greater baseline uncertainty because icing affects flow over reference sensors which would result in underestimation of convective heat losses. Mean baseline LWC_{NEV} (0.04 g m^{-3}) is greater than $MDS\ LWC_{NEV}$ (0.02 g m^{-3}) for SNOWIE flights which were often affected by appreciable instrument icing.

TWC calculations use a term that represents the energy expended for the vaporization of liquid water (L_W; equation 2.3) which neglects that sensible and latent heats are phase dependent. In mixed and ice phase cloud, the simplification can result in as great as 12% overestimation of TWC. Nonetheless, L_W (instead of L_i) is typically used because the relative ratio of liquid water to ice mass in often unknown. TWC could be selectively calculated with L_i during penetrations that are confirmed to be in all ice cloud.

Collection efficiency effects can also cause TWC and LWC underestimation. Droplets less than 30 μm VMD are more efficiently collected by the rod shaped LWC sensor because it causes less flow disruption than the TWC sensor. The TWC sensor has higher collection efficiencies for droplets larger than 30 μm because larger droplets are prone to splattering when contacting the LWC sensor (Korolev et al., 1998; Strapp et al., 2003; Schwarzenboeck et al., 2009). Sensor saturation occurs when insufficient power

is available to evaporate collected particles and can cause underestimation of both TWC and LWC (Emery et al., 2004).

Ice particles impacting the TWC sensor can rebound and be swept away which causes TWC to be underestimated. A modified deep cone TWC sensor was developed to mitigate ice rebounding and was shown to measure 3 times more IWC than the standard sensor design (Korolev et al., 2013). The LWC sensor is designed to minimally interact with ice particles but interactions between ice and the LWC sensor can cause LWC overestimation equal to 11% IWC (Korolev et al., 1998).

Nevzorov measurements taken in different cloud phases and drizzle conditions are presented. During the liquid cloud and drizzle periods, droplet collection efficiency considerations can account for differences between LWC and TWC.

It is expected that droplet collection efficiency considerations will cause TWC to be ~23% less than LWC during the liquid cloud penetration. Data show that percent TWC vs. LWC difference is similar (-22% difference). During the drizzle period, TWC is 67% greater than LWC. Differences in collection efficiency are expected to cause a 60% TWC vs. LWC difference when operating in conditions dominated by 150 μm drops (Korolev et al., 1998; Strapp et al., 2003; Schwarzenboeck et al., 2009). 2DS buffers indicate that very few ice particles were present so the majority of LWC/TWC difference is likely due to collection efficiency considerations.

During an ice cloud penetration, LWC measurements were greater than MDS LWC which is likely due to ice particle interactions with the LWC sensor. Korolev et al. (1998) estimated that ice interactions can cause LWC error equal to 11% IWC. Actual mean percent difference of LWC vs. TWC is 12%. TWC measurements are less than 0.7 g m^{-3} so TWC sensor pooling in likely not an issue (Korolev et al., 2013). It is not possible to give an overall estimate of TWC/IWC error due to unknowns regarding ice rebounding and TWC ice collection efficiency.

It is difficult to estimate Nevzorov uncertainty in mixed phase conditions. Droplet collection efficiency considerations are expected to cause less than 8% underestimation of LWC or TWC. It is not possible to estimate LWC and IWC error caused by interactions between the LWC sensor and ice particles without an accurate independent measurement of IWC. Furthermore, it is not possible to estimate total error in TWC and IWC because TWC ice collection efficiency and the effects of ice rebounding are poorly understood.

CDP measurements can be affected by two types of coincidence error which can cause error in sizing, counting, concentration, and LWC. Standard coincidence occurs when multiple droplets are within the standard sample area and only affects CDP measurements in high droplet concentrations. Extended coincidence occurs when droplets are within both the standard and extended sample areas (Lance et al., 2010). Extended coincidence is capable of affecting CDP measurements in lower droplet

concentrations but the UWKA CDP features a sizer pinhole mask designed to reduce the occurrence of extended coincidence (Lance et al., 2012).

PACMICE and SNOWIE data are used to compare $\mathrm{LWC_{CDP}}$ and $\mathrm{LWC_{NEV}}$ to further investigate error sources for both instruments. Data were filtered to include penetrations of liquid only cloud to decrease error caused by ice interactions with the Nevzorov LWC sensor. It is expected that CDP missizing, miscounting, and Nevzorov collection efficiency considerations should cause $\mathrm{LWC_{CDP}}$ vs. $\mathrm{LWC_{NEV}}$ percent difference no greater than 15% but actual mean LWC difference is near 20%. It is unlikely that coincidence effects cause the discrepancy between the actual and expected percent LWC difference because 99% of points have concentrations less than 500 cm^{-3}.

Droplet generator tests used a single droplet velocity that is ~30% of typical UWKA airspeed. It is possible that CDP sizing accuracy, counting accuracy, or SA varies with airspeed which could explain the discrepancy between estimated and actual percent $\mathrm{LWC_{CDP}}$ vs. $\mathrm{LWC_{NEV}}$. Additional droplet generator tests that use greater droplet velocities could be conducted to investigate if CDP performance varies with airspeed.

5 - Thesis summary

Cloud water content and droplet size distribution measurements are useful for studies of cloud microphysical processes and cloud radiative properties. Hotwire devices including the King, LWC-100, SEA, and Nevzorov probes are commonly used to provide measurements of bulk liquid water content. The FSSP and CDP are optical particle counters that provide measurements of individual droplet size and by extension, full droplet size distributions from which moments may be calculated.

The Nevzorov provides measurements of total condensed and liquid water content by relating thermodynamic principles to the amount of sensor cooling caused by particle evaporation. Collection efficiency effects are one of the largest sources of uncertainty in Nevzorov measurements. Droplet collection efficiency has been studied and parameterized by several researchers (Korolev et al., 1998; Strapp et al., 2003; Schwarzenboeck et al., 2009). A parameterization of ice collection efficiency has not been developed because ice particles are difficult to produce in laboratory settings and independent in-situ ice water content measurements are unreliable.

Korolev et al. (2013) showed that ice particles can bounce out of the total water content collector leading to ice water content underestimation. A modified ‘deep cone’ total water content collector was developed to mitigate ice rebounding and increased ice water content measurements by a factor of 3 compared to standard ‘shallow cone’ measurements (Korolev et al., 2013). Both the liquid and total water content sensors

can be affected by saturation that occurs when insufficient power is available to evaporate all collected particles (Korolev et al., 1998; Emery et al., 2004). Sensor saturation results in underestimation of liquid and total water content. The liquid water content collector is designed to minimally interact with ice particles but it is estimated that residual ice interaction causes liquid water content overestimation on the order of 11% of ice water content (Korolev et al., 1998).

Convective heat losses cause collector sensor cooling that leads to overestimation of liquid and total water content (King et al., 1978). The Nevzorov probe monitors power supplied to a reference sensor that is used to determine the amount of cooling due to convective losses. The convective heat loss coefficient is sensitive to changes in airspeed and/or density resulting in liquid and total water content baseline drift. A convective heat loss calibration method was developed that uses clear air data from University of Wyoming King Air calibration flights and a first-degree surface fit to estimate dependence on indicated airspeed and pressure. The effectiveness of the calibration method is tested using points devoid of cloud and precipitation. In the absence of instrument icing, the calibration results in total and liquid water content uncertainty of 0.02 g m^{-3} and 0.03 g m^{-3} respectively. Minimum detectable total and liquid water content are estimated to be 0.01 g m^{-3} and 0.02 g m^{-3}.

Nevzorov measurements, CDP measurements, and 2DS buffer images are used to explore Nevzorov uncertainty in liquid cloud, ice cloud, mixed phase cloud, and drizzle conditions. Differences between liquid and total water content can be explained by

differences in droplet collection efficiency during the liquid cloud and drizzle periods. During the ice phase period, liquid water content is greater than what can be attributed to baseline drift. The observed error in liquid water content can be explained by interactions between ice particles and the liquid water content sensor. It is difficult to estimate liquid, total, and ice water content error in mixed phase conditions due to lack of independent ice water content measurements and unknowns regarding total water content sensor ice collection efficiency and ice rebounding.

The CDP is an optical particle counter that measures droplet sizes and counts. From CDP measurements, droplet size distributions and higher order moments can be calculated. Droplets that pass through the CDP's open path laser scatter light in the forward direction that is collected and focused onto a pair of photodetectors. Measurements of droplet size are provided by relating detector response to Mie theory. Optical component misalignment, inhomogeneity in laser intensity, and coincidence error can lead to errors in both sizing and counting (Wendisch et al., 1996). These errors affect concentration, liquid water content, and higher order moments of droplet size distributions. Error in concentration and liquid water content can also be caused by uncertainty in sample area measurements (Wendisch et al., 1996).

A droplet generating calibration system was built to test sizing and counting accuracy at discrete locations across the sample area of the UWKA CDP and to provide measurements of sample area dimensions. Calibrations were conducted using droplets of 9, 17, 24, 29, 34, 38, and 46 μm diameter. The calibrations show that when sizing

accuracy is averaged for all sample locations, the CDP undersizes 9 μm droplets by ~1.5 um and measures all other droplet sizes to within 1 μm. Sizing accuracy is locationally dependent which results in artificial broadening of distributions and can complicate droplet size distribution interpretation. Missizing causes less than 1.5 μm error in mean diameter, effective diameter, or volume-weighted mean diameter for all tested droplet sizes. The calibrations show that 9 μm droplets are subject to less than 6% undercounting and all other droplet sizes are subject to less than 3% count error. Calibrations indicate that 9 μm droplets are subject to as great as 42% liquid water content underestimation. Absolute liquid water content error is less than 15% for all other droplet sizes.

The measured sample area from these tests is ~0.27 mm^2 and varies ~0.03 mm^2 depending on droplet diameter. Sample area used in calculations of concentration and liquid water content could be provided by either a fixed value of 0.27 mm^2 or a variable value that employs a second-degree polynomial fit of sample area dependence on droplet size. Concentration and liquid water content are calculated for three Poissonian droplet size distributions using fixed and variable sample area. Using the two types of sample area estimates result in less than 6% difference in concentration and LWC so it is most logical to use a fixed sample area of 0.27 mm^2.

Liquid phase PACMICE and SNOWIE data are used to compare measurements of liquid water content from the CDP and Nevzorov. For droplets larger than 20 μm, it is expected that CDP component misalignment, inhomogeneity in laser intensity (both

based on calibration results), and Nevzorov droplet collection efficiency considerations should result in less than 15% difference between CDP and Nevzorov liquid water content. Actual percent difference in liquid water content is on the order of 20%. The discrepancy between estimated and actual percent difference in liquid water content is unlikely to be caused by coincidence error because 99% of data points have concentrations less than 500 cm^{-3}; a range that is not impacted by coincidence (Lance et al., 2012; Sulskis, 2016).

It is possible that CDP electronic response time limitations contribute to the discrepancy between estimated and actual percent difference in CDP and Nevzorov liquid water content. CDP calibrations used a droplet velocity that is ~30% of typical UWKA airspeed so the tests did not provide information regarding how missizing, miscounting, and sample area vary with airspeed. Additional CDP calibrations using higher droplet velocity are required to further investigate if an airspeed dependence in sizing accuracy, counting accuracy, and/or SA could account for the discrepancy between the predicted and actual percent difference of CDP vs. Nevzorov liquid water content.

6. – References

Baker, M. B., R. G. Corbin, and J. Latham, 1980: *The influence of entrainment on the evolution of cloud droplet spectra: I. A model of inhomogeneous mixing*. Q. J. R. Meteorol. Soc., 106, 581–598, doi:10.1002/qj.49710644914. http://doi.wiley.com/10.1002/qj.49710644914.

Baumgardner, D., 1983: An Analysis and Comparison of Five Water Droplet Measuring Instruments. *J. Clim. Appl. Meteorol.*, **22**, 891–910, doi:10.1175/1520-0450(1983)022<0891:AAACOF>2.0.CO;2. http://journals.ametsoc.org/doi/abs/10.1175/1520-0450%281983%29022%3C0891%3AAAACOF%3E2.0.CO%3B2.

Baumgardner, D., W. Strapp, and J. E. Dye, 1985: Evaluation of the Forward Scattering Spectrometer Probe. Part II: Corrections for Coincidence and Dead-Time Losses. *J. Atmos. Ocean. Technol.*, **2**, 626–632, doi:10.1175/1520-0426(1985)002<0626:EOTFSS>2.0.CO;2.

Bergeron, T., 1935: *On the physics of cloud and precipitation*. Proc. 5th Assembly U.G.G.I. Lisbon. Vol. 2, 156.

Blanchard, D. C., 1950: The behavior of water drops at terminal velocity in air. Transactions - American Geophysical Union, **31**, 836. DOI: 10.1029/TR031i006p0083

Blyth, A. M., 1993: *Entrainment in Cumulus Clouds*. J. Appl. Meteorol., **32**, 626–641, doi:10.1175/1520-0450(1993)032<0626:EICC>2.0.CO;2.

Bowen, E.G., 1950: The Formation of Rain by Coalescence. *Australian Journal of Chemistry*, **32**, pp.193-213.

Brenguier, J. L., 1988: Effects of Coincidence on Measurements with a Forward Scattering Spectrometer Probe. *J. Atmos. Ocean. Technol.*, **5**, 823–832, doi:10.1175/1520-0426(1988)005<0823:EOCOMW>2.0.CO;2.

Brenguier, J. L., 1989: Coincidence and Dead-Time Corrections for Particles Counters. Part II: High Concentration Measurements with an FSSP. *J. Atmos. Ocean. Technol.*, **6**, 585–598, doi:10.1175/1520-0426(1989)006<0585:CADTCF>2.0.CO;2.

Cotton, R. J., and Coauthors, 2013: The effective density of small ice particles obtained from in situ aircraft observations of mid-latitude cirrus. *Q. J. R. Meteorol. Soc.*, **139**, 1923–1934, doi:10.1002/qj.2058.

Droplet Measurement Technologies, 2014: Cloud Droplet Probe (CDP-2). http://www.dropletmeasurement.com/products/airborne/CDP-2.

Dye, J. E., and D. Baumgardner, 1984: Evaluation of the Forward Scattering Spectrometer Probe. Part I: Electronic and Optical Studies. *J. Atmos. Ocean. Technol.*, **1**, 329–344, doi:10.1175/1520-0426(1984)001<0329:EOTFSS>2.0.CO;2.

Emery, E. F., et al., 2004: Ice Particle Impact on Cloud Water Content Instrumentation. doi:10.2514/6.2004-731.

Findeisen, W., 1938: *Die kolloidmeteorologischen Vorgänge bei der Niederschlagsbildung*. Met. Z. 55. 121.

Henderson B., and Sellers, 1984: A new formula for latent heat of vaporization of water as a function of temperature. *Q. J. R. Meteorol. Soc.*, **110**, 1186–1190, doi:10.1002/qj.49711046626.

JAI, 2017: CV-A10CL. http://www.jai.com/en/products/cv-a10cl

King, W. D., D. A. Parkin, and R. J. Handsworth, 1978: A Hot-Wire Liquid Water Device Having Fully Calculable Response Characteristics. *J. Appl. Meteorol.*, **17**, 1809–1813, doi:10.1175/1520-0450(1978)017<1809:AHWLWD>2.0.CO;2. http://journals.ametsoc.org/doi/abs/10.1175/1520-0450(1978)017%3C1809:AHWLWD%3E2.0.CO;2.

Koenig, L. R., and F. W. Murray, 1977: The rime-splintering hypothesis of cumulus glaciation examined using a field-of-flow cloud model. *Q. J. R. Meteorol. Soc.*, **103**, 585–606, doi:10.1002/qj.49710343805.

Köhler, H., 1936: The nucleus in and the growth of hygroscopic droplets. *Trans. Faraday Soc.*, **32**, 1152–1161, doi:10.1039/TF9363201152. http://xlink.rsc.org/?DOI=TF9363201152.

Korolev, A. V., 1994: A study of bimodal droplet size distributions in stratiform clouds. *Atmos. Res.*, **32**, 143–170, doi:10.1016/0169-8095(94)90057-4.

Korolev, A. V., S. V. Kuznetsov, Y. E. Makarov, and V. S. Novikov, 1991: Evaluation of measurements of particle size and sample area from optical array probes. *J. Atmos. Ocean. Technol.*, **8**, 514–522, doi:10.1175/1520-0426(1991)008<0514:EOMOPS>2.0.CO;2.

Korolev, A., J. W. Strapp, G. A. Isaac, and E. Emery, 2013: Improved airborne hot-wire measurements of ice water content in clouds. *J. Atmos. Ocean. Technol.*, **30**, 2121–2131, doi:10.1175/JTECH-D-13-00007.1.

Korolev, A. V, J. W. Strapp, G. A. Isaac, and A. N. Nevzorov, 1998: The Nevzorov airborne hot-wire LWC-TWC probe: Principle of operation and performance characteristics. *J. Atmos. Ocean. Technol.*, **15**, 1495–1510, doi:10.1175/1520-0426(1998)015<1495:Tnahwl>2.0.Co;2.

Lamb and Verlinde, 2011: Physics and Chemistry of Clouds. Cambridge University Press, 584 pp.

Lance, S., 2012: Coincidence errors in a cloud droplet probe (CDP) and a cloud and aerosol spectrometer (CAS), and the improved performance of a modified CDP. *J. Atmos. Ocean. Technol.*, **29**, 1532–1541, doi:10.1175/JTECH-D-11-00208.1.

Lance, S., C. A. Brock, D. Rogers, and J. A. Gordon, 2010: Water droplet calibration of the Cloud Droplet Probe (CDP) and in-flight performance in liquid, ice and mixed-phase clouds during ARCPAC. *Atmos. Meas. Tech.*, **3**, 1683–1706, doi:10.5194/amt-3-1683-2010. http://www.atmos-meas-tech.net/3/1683/2010/.

MicroFab Tech.: Low Temperature Dispensing Devices. http://www.microfab.com/dispensing-devices/low-temp-devices

Morrison, H., and G. Gettelman, 2008: A new two-moment bulk stratiform cloud microphysics scheme in the community atmosphere model, version 3 (CAM3). Part I: Description and numerical tests. *J. Clim.*, **21**, 3642–3659, doi:10.1175/2008JCLI2105.1.

Morrison, H., G. Thompson, and V. Tatarskii, 2009: Impact of Cloud Microphysics on the Development of Trailing Stratiform Precipitation in a Simulated Squall Line: Comparison of One- and Two-Moment Schemes. Mon. Weather Rev., 137, 991–1007, doi:10.1175/2008MWR2556.1.

Mason, B. J., and C. W. Chien, 1962: Cloud-droplet growth by condensation in cumulus. *Q. J. R. Meteorol. Soc.*, **88**, 136–142, DOI: 10.1002/qj.49708837603.

McFarquhar, G. M., et al., 2017: Processing of Ice Cloud In-Situ Data Collected by Bulk Water, Scattering and Imaging Probes: Fundamentals, Uncertainties and Efforts towards Consistency. *American Meteorological Society*

MicroFab Inc., MicroJet Cleaning Guide. http://www.microfab.com/images/pdfs/MJCleaningGuide_Ver7.pdf.

Mossop, S. C., 1970: Concentrations of Ice Crystals in Clouds. *Bull. Am. Meteorol. Soc.*, **51**, 474–479, doi:10.1175/1520-0477(1970)051<0474:COICIC>2.0.CO;2. http://journals.ametsoc.org/doi/abs/10.1175/1520-0477(1970)051%3C0474:COICIC%3E2.0.CO;2.

Mossop, S. C., and J. Hallett, 1974: *Ice Crystal Concentration in Cumulus Clouds : Influence of the Drop Spectrum*. American Association for the Advancement of Science., **186**, 632–634.

MicroFab Tech.: JetDrive III. http://www.microfab.com/images/pdfs/v.4/jetdrive3_mf5.pdf

MicroFab Tech.: Pneumatics & Temperature Controllers. http://www.microfab.com/images/pdfs/pneumatics_mf4.pdf

Nagel, D., U. Maixner, W. Strapp, and M. Wasey, 2007: Advancements in techniques for calibration and characterization of in situ optical particle measuring probes, and applications to the FSSP-100 probe. *J. Atmos. Ocean. Technol.*, **24**, 745–760, doi:10.1175/JTECH2006.1.

Perrin, T., J. L. Brenguier, and T. Bourrianne, 1998: Modeling coincidence effects in the Fast-FSSP with a Monte Carlo model. *Preprints, Conf. on Cloud Physics, Amer. Meteor. Soc., Everett, WA*, 112–115.

Schwarzenboeck, A., G. Mioche, A. Armetta, A. Herber, and J.-F. Gayet, 2009: Response of the Nevzorov hot wire probe in clouds dominated by droplet conditions in the drizzle size range. *Atmos. Meas. Tech.*, **2**, 779–788, doi:10.5194/amt-2-779-2009. http://www.atmos-meas-tech.net/2/779/2009/.

Scott, W. T., 1968: Analytic Studies of Cloud Droplet Coalescence I. *J. Atmos. Sci.*, **25**, 54–65, doi:10.1175/1520-0469(1968)025<0054:ASOCDC>2.0.CO;2. http://dx.doi.org/10.1175/1520-0469(1968)025%3C0054:ASOCDC%3E2.0.CO;2%5Cnhttp://journals.ametsoc.org/doi/abs/10.1175/1520-0469(1968)025%3C0054:ASOCDC%3E2.0.CO;2.

Simco-Ion, 2013: Ionizing Air Cartridge. http://technology-ionization.simco-ion.com/Products/IonizingGunsNozzlesCartridges/IonizingAirCartridge.aspx#17701402-overview

SkyPhysTech: Operating Manual Nevzorov hot wire LWC / TWC Probe.

Squires, P., 1952: The growth of Cloud Drops by Condensation. I. General Characteristics. *Australian Journal of Scientific Research*, **5**, 59, DOI: 10.1071/PH520059

Strapp, J. W., et al., 2003: Wind tunnel measurements of the response of hot-wire liquid water content instruments to large droplets. *J. Atmos. Ocean. Technol.*, **20**, 791–806, doi:10.1175/1520-0426(2003)020<0791:WTMOTR>2.0.CO;2.

Sulskis J. A., 2016: A comparison and survey of the measured cloud liquid water content and an analysis of the bimodal droplet spectra observed during COPE-MED. *ProQuest*: 10169205

Taylor, J. W., et al., 2016: Observations of cloud microphysics and ice formation during COPE. *Atmos. Chem. Phys.*, **16**, 799–826, doi:10.5194/acp-16-799-2016.

ThorLabs: APT Stepper Motor Controllers. https://www.thorlabs.us/newgrouppage9.cfm?objectgroup_id=1704

ThorLabs: Kinesis Software. https://www.thorlabs.com/newgrouppage9.cfm?objectgroup_id=10285

ThorLabs: Linear Translation Stages. https://www.thorlabs.us/newgrouppage9.cfm?objectgroup_id=2297

Warner, J., 1973: The Microstructure of Cumulus Cloud: Part IV. The Effect on the Droplet Spectrum of Mixing Between Cloud and Environment. *J. Atmos. Sci.*, **30**, 256–261, doi:10.1175/1520-0469(1973)030<0256:TMOCCP>2.0.CO;2. http://dx.doi.org/10.1175/1520-0469(1973)030%3C0256:TMOCCP%3E2.0.CO%5Cn2.

Wegener, A., 1911: Thermodynamik der Atmosphare. Leipzig, **331**

Wendisch, M., A. Keil, and A. V. Korolev, 1996: FSSP characterization with monodisperse water droplets. *J. Atmos. Ocean. Technol.*, **13**, 1152–1165, doi:10.1175/1520-0426(1996)013<1152:FCWMWD>2.0.CO;2.

Zelinka, M. D., and D. L. Hartmann, 2010: Why is longwave cloud feedback positive? *J. Geophys. Res. Atmos.*, **115**, 1–16, doi:10.1029/2010JD013817.

Zender, C., 2002: Particle size distributions: theory and application to aerosols, clouds, and soils. *2008-01-25)[2010-02-10]. Http//Dust. Ess. Uci. Edu/Facts …*,. http://scholar.google.com/scholar?hl=en&btnG=Search&q=intitle:Particle+Size+Distributions:+Theory+and+Application+to+Aerosols+,+Clouds+,+and+Soils#0.